Control Engineering Practice 165 (2025) 106597

Contents lists available at ScienceDirect

Control Engineering Practice

journal homepage: www.elsevier.com/locate/conengprac

# Locomotive wheel-slip control with slip ratio reference adaptation using model-based estimation

Charl V. van de Merwe [a], Johan D. le Roux [a,*], David J.N. Limebeer [b]

[a] Department of Electrical, Electronic and Computer Engineering, University of Pretoria, Pretoria, South Africa
[b] Department of Electrical and Information Engineering, University of Witwatersrand, Johannesburg, South Africa

ARTICLE INFO

*Keywords:*
Locomotives
Modelling
Parameter estimation
Adaptive control
Railways

ABSTRACT

This paper investigates the wheel-slip control of locomotive traction systems in the presence of uncertain wheel-rail rolling contact conditions. A linear estimator is used to produce estimates of the wheels' slip ratios and adhesion coefficients. These estimates are used as part of a slip ratio reference adaptation scheme that provides a reference to an adaptive PI controller. The control architecture is intentionally designed to be suitable for practical deployment in industrial settings, where simplicity and reliability are essential. A detailed pitch-plane simulation model is used to validate the controller performance. The results indicate that the estimator-controller combination can prevent unstable slip over a wide range of adhesion conditions, thereby preventing damage to the wheels and rail while ensuring maximum adhesion.

## 1. Introduction

Slip control aims to maintain good wheel-rail adhesion and prevent unstable slip, defined here as operation in the region of the $\mu$–$\lambda$ curve where the slope becomes negative. The prolonged application of excessive traction torque causes unstable wheel slip. If the drive torque is not reduced during slipping, the wheel angular velocity will increase with an accompanying reduction in traction. Unstable slip also leads to accelerated wheel and rail damage (Park et al., 2009; Wang et al., 2019).

The traction limit is dependent on the adhesion forces between the wheels and rail, described by:

$$F_a = \mu F_N, \tag{1}$$

where $\mu$ is the adhesion coefficient (coefficient of friction), and $F_N$ is the wheel-rail normal force. The adhesion coefficient is dependent on the wheel-rail slip ratio (Spiryagin et al., 2017) given by:

$$\lambda = \pm(r\,\omega_d - v_V)/v_V, \tag{2}$$

where $v_V$ is the locomotive velocity, $\omega_d$ is the driven-wheel angular velocity, and $r$ is the wheel radius. The sign is positive during traction, and negative under braking. The characteristic curves relating the adhesion coefficient to the slip ratio are shown in Fig. 1, from which it is evident that the slip ratio should be kept below the peak to maximize adhesion and prevent unstable slip. The detailed shape of these curves is determined by environmental factors, such as temperature and humidity, as well as the normal force (He et al., 2018). Slip control is complicated by the fact that the adhesion coefficient cannot be measured directly (Pichlik, 2019), and the peak slip ratio (corresponding to the maximum adhesion) is typically unknown. The target slip ratio operating point is in the stable region near the peak and to the left of it (Pichlik, 2019).

Fig. 2 presents a simple slip controller. The desired torque setpoint $T^*$ is calculated for a specified notch (specifying the desired locomotive power output), and the estimated driven-wheel surface velocity $\hat{v}_d = r\,\hat{\omega}_d$ (Spiryagin et al., 2017). The torque setpoint is then modified by the reaction torque, $T_{\text{react}}$, which should increase during unstable slip: when the estimated slip ratio exceeds the slip ratio reference ($\hat{\lambda} > \lambda_R$) (Pretagostini et al., 2020; Savitski et al., 2018; Spiryagin et al., 2017). Anti-windup is needed to reduce the reaction torque if the slip ratio is smaller than the reference (Pretagostini et al., 2020; Savitski et al., 2018).

Generally, unknown rolling-contact conditions make determining the optimal slip ratio difficult. In addition, providing an accurate slip ratio reference is complicated by the locomotive velocity determination if all the wheelsets are driven (Pichlik, 2019), especially at low speeds (Spiryagin et al., 2017). These challenges make it difficult to use continuous torque modulation approaches, such as proportional integral (PI), linear quadratic regulators (LQR), sliding mode control (SMC), robust, and model predictive controllers (MPC) (Pretagostini et al., 2020). Alternative approaches are discrete torque modulation with rule-based (also called dynamic threshold-based) (Wang et al.,

* Corresponding author.
*E-mail address:* derik.leroux@up.ac.za (J.D. le Roux).

https://doi.org/10.1016/j.conengprac.2025.106597
Received 25 February 2025; Received in revised form 18 September 2025; Accepted 19 September 2025
Available online 29 September 2025

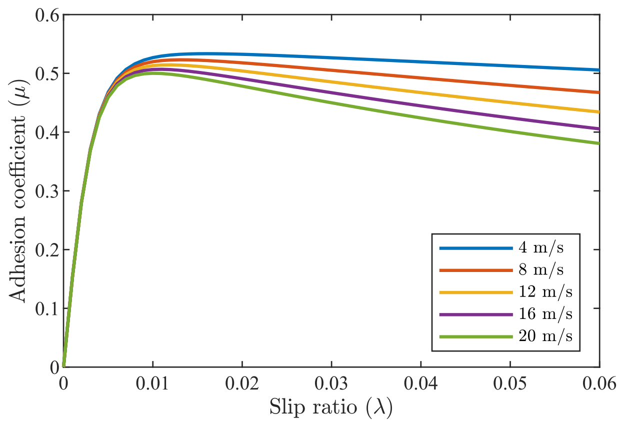


**Fig. 1.** Adhesion coefficient versus slip ratio at different locomotive velocities at *dry* adhesion conditions.

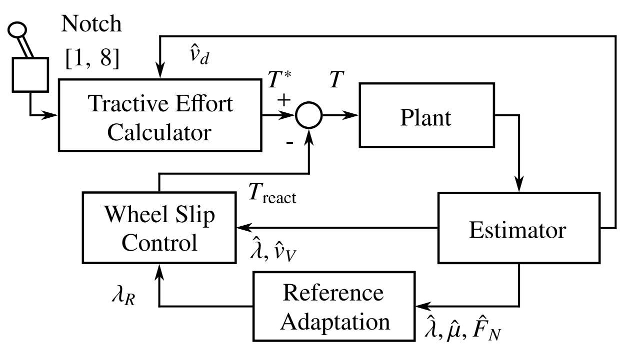


**Fig. 2.** Slip control using slip ratios as inputs.

2016, 2019), fuzzy-logic (Djukić et al., 2010; Sadr et al., 2016; Tian et al., 2014), or neural-network controllers (Pretagostini et al., 2020).

Rule-based and fuzzy controllers have traditionally been used in industrial applications, especially automotive anti-lock braking systems (ABS), since they do not require precise system models and can be tuned from empirical data, albeit an iterative and intensive process (Pretagostini et al., 2020; Savitski et al., 2018). Fuzzy logic controllers have demonstrated superior performance compared to PI controllers with constant gains, especially in the presence of modelling and estimation errors (Tian et al., 2014). As an added complication, PI controllers can produce oscillatory wheel-slip behaviour (Savitski et al., 2018).

The introduction of electric vehicles (EVs) with electro-hydraulic braking systems offers more accurate torque control and higher computational power. It has sparked a renewed interest in slip control with continuous torque modulation (Tavernini et al., 2020). Continuous torque modulation may produce superior performance if an optimal slip ratio reference can be generated.

PI controllers are typically tuned for a specific linear model that may make them poorly suited to variable wheel-rail conditions (Savitski et al., 2018). SMC is an attractive alternative since it improves robustness against model uncertainties (Kayacan et al., 2009; Savitski et al., 2018), but can suffer from chattering (rapid control actuation) (Pretagostini et al., 2020). Good robustness and reduced chattering can be achieved using an integral SMC (Savitski et al., 2018).

LQRs have been attempted but are sensitive to modelling errors (Pretagostini et al., 2020). Classical robust ($\mathcal{H}^\infty$) controllers achieve robust performance by handling the uncertainty explicitly (Pretagostini et al., 2020), but are more complex to compute (Green & Limebeer, 2012). $\mathcal{H}^\infty$ controllers generally assume a fixed longitudinal slip stiffness, from which the adhesion force is computed. However, the large range of variation in slip stiffness makes it difficult to find an optimal $\mathcal{H}^\infty$ controller (Tavernini et al., 2020).

MPC offers good robustness and tracking performance (50% faster slip recovery than a rule-based controller) but represents a high computational load (Pretagostini et al., 2020). In electric vehicles, the choice of implementation time step significantly impacts the performance of the controller, often more than the selected control method (Tavernini et al., 2020). A possible solution is an explicit non-linear MPC, which requires a fraction of the computing time (Tavernini et al., 2020).

While 'advanced' controllers may improve reference tracking and robustness against model variabilities and non-linearity, they still depend on finding the optimal slip ratio reference. A constant reference is used in many automotive applications (Park et al., 2009; Savitski et al., 2018). As shown in Fig. 1, the adhesion coefficient drops with an increase in locomotive velocity (Chang et al., 2019), and the peak slip ratio decreases (Picasso et al., 2018). Therefore, an improved method can use a pseudo-static curve that varies the slip ratio reference according to the locomotive velocity (Kayacan et al., 2009). However, this pseudo-static curve is computed for a specific friction condition and is not always optimal.

Assuming estimates of the adhesion coefficient and slip ratio and their derivatives can be found, these could be used to find the varying peak slip ratio to update the reference in real-time. In Park et al. (2009), fuzzy logic is used to calculate the variation of the derivative of the adhesion coefficient with respect to the slip ratio, $\Delta(\dot{\lambda}, \dot{\mu})$. This parameter is decreased if $d\hat{\mu}/d\hat{\lambda} < 0$ and increased otherwise; $\mu$ is the actual adhesion coefficient ($\mu = \mu_{\text{actual}}$). The rule: $\lambda_R^k = \lambda_R^{k-1} + \Delta(\dot{\lambda}, \dot{\mu})$, can be used to generate a discrete slip ratio reference at sample $k$.

Instead of using $d\hat{\mu}/d\hat{\lambda}$ directly, the slope of the characteristic curves, as shown in Fig. 1, can be approximated. In the first approach, the partial derivative of the locomotive acceleration with respect to the slip ratio is used (Zengin et al., 2020). In the second, the partial derivative of adhesion force with respect to the slip ratio is used (Savitski et al., 2018). In both, the partial derivates are found with recursive least squares. A slip ratio reference is generated if a change in the sign of the slope is detected by taking the mean of the last few samples of the slip ratio (Savitski et al., 2018).

If a model matching the shape of the characteristic curve is found, the peak slip ratio could be derived from it. In He et al. (2018), maximum likelihood estimation is performed using estimates for the adhesion coefficient and slip ratio to find the parameters of the Burckhardt contact model. A related approach is seen in Caporale et al. (2013), where a simplified nonlinear approximation of the adhesion curve is introduced, inspired by the Polach model, and used within an adaptive control framework to estimate and exploit the maximum available adhesion.

Slip ratio reference generation and slip control require accurate estimates of the adhesion coefficient and slip ratio, as shown in Fig. 2. The locomotive velocity, $v_V$, must be determined accurately to produce longitudinal slip ratio estimates. The locomotive velocity could be measured directly with a Doppler radar or a lidar sensor, but these systems are expensive and require additional filtering (Ararat & Söylemez, 2017; Spiryagin et al., 2017). The velocity could also be estimated using a Kalman or Rao-Blackwellized particle filter with longitudinal acceleration and GPS position measurements (Berntorp, 2016), but GPS may not be reliable (Ararat & Söylemez, 2017). A possible alternative is estimation using an inverse locomotive model and measurements of the time shift of the rail vibration between two wheelsets of a bogie (Mei & Li, 2010). The velocity could be estimated using wheel angular rate measurements (Ararat & Söylemez, 2017; Kun et al., 2006). However, doing so assumes a constant longitudinal stiffness, rendering it inaccurate during significant variations in adhesion conditions.

The adhesion coefficient can be estimated directly (Spiryagin et al., 2011) but is generally calculated indirectly from adhesion force and normal force estimates ($\hat{\mu} = \hat{F}_a/\hat{F}_N$). In many applications, a constant normal force is used (Ararat & Söylemez, 2017; Kun et al., 2006), but a pitch-plane mode can be used to estimate it (Rezaeian et al., 2015). The longitudinal adhesion force can be estimated in a model-based approach using only the wheelset rotational dynamics (Ohishi et al., 1998; Pichlik & Zdenek, 2018; Rezaeian et al., 2015).

Choosing the dynamics to include in a Kalman filter is essential because it directly impacts the accuracy and reliability of the estimated states. In Van de Merwe and Le Roux (2022), the locomotive longitudinal, vertical, pitch and wheelset rotational dynamics are used to produce estimates of the longitudinal slip ratios and adhesion forces of each wheelset. This approach was based on similar work in Charles et al. (2008), Ward et al. (2011) and Ward et al. (2012), where the lateral adhesion forces were calculated from a model including the lateral dynamics of the vehicle body and the lateral and yaw degrees of freedom of the bogies. A Kalman-Bucy filter is used, and the estimation model is a rigid body system floating on a series of contact forces. The lateral adhesion forces are relevant for condition monitoring. Although unstable lateral slip will reduce the longitudinal adhesion force (Ndiaye et al., 2022), an estimator that includes the wheelset rotational dynamics is sufficient to capture the variability without including the lateral dynamics.

The contribution of this article is the combination of a novel estimator, a slip controller, and a slip ratio reference adaptation scheme. The combined system is simple to implement practically on an industrial locomotive, as complex locomotive modelling is not required to construct the estimator. The requirements for the estimator are measurements of the longitudinal acceleration and rail angle via an inertial measurement unit, as well as a separate measurement of the locomotive velocity. The requirement for the slip controller is accurate individual wheelset torque control, which is common on modern locomotives. The proposed combined estimator, controller and reference adaptation system yields satisfactory control of wheel-slip in simulation. The estimator produces an adhesion coefficient estimate that converges within 15 ms, which allows the slip ratio reference adaptation to find the adhesion level from which the references are derived. Compared to a constant slip ratio reference, the proposed adaptive method improves braking distance by 3% in low adhesion conditions and up to 13% in very low conditions.

Section 2 presents and elaborates on the simulation model given in Van de Merwe and Le Roux (2022). Section 3 describes the wheel-rail contact dynamics. The same estimation model as in Van de Merwe and Le Roux (2023) is presented in Section 4, but a more rigorous approach to deriving the reduced order wheelset model is used. Section 5 presents a PI controller to prevent slip in the rear wheelset and a differential speed controller to control the speed of the other wheelsets. Section 6 presents the slip ratio reference adaptation method, which provides the reference to the PI controller. The estimator, reference adaptation and slip controller are combined and used in traction and braking simulations in Section 7 to test the performance of the system. The paper is concluded in Section 8.

## 2. Simulation model

The locomotive dynamics are modelled using Newtonian mechanics (given in this section) and the wheel-rail contact mechanics (Section 3) (Ward et al., 2011). Many existing studies, such as Caporale et al. (2013), Kayacan et al. (2009) and Park et al. (2009), use single-axle wheelset models and neglect dynamic effects such as normal force redistribution between wheelsets. A Bo-Bo (two wheelsets per bogie) diesel locomotive is modelled here in detail. As shown in Fig. 3, the simulation model includes the longitudinal, vertical, pitch and wheelset rotational dynamics. It is assumed that the wheels do not lose contact with the rails, i.e., the wheelsets have no vertical displacement (Charles et al., 2008; Spiryagin et al., 2017). The model neglects vertical dynamics from rail irregularities, as modern rails are generally smooth and such excitations are negligible. The SAE sign convention, as shown in Fig. 3, is used throughout.

**Table 1**
Modelling parameters, in order of appearance.

| Symbol | Description |
|---|---|
| $m_V, m_{Bi}, m_{Wij}$ | Vehicle body, bogies & wheelset masses. |
| $x_V, x_{Bi}, x_{Wij}$ | Vehicle body, bogie & wheelset longitudinal displacements. |
| $F_{Ti}$ | Traction rod forces. |
| $F_{PXij}$ | Primary suspension longitudinal forces. |
| $F_{aLij}, F_{aRij}$ | Left & right wheel adhesion forces. |
| $\theta_V$ | Vehicle body pitch angle. |
| $F_{gV}, F_{gBi}, F_{gWij}$ | Vehicle body, bogie & wheelset gravitational forces. |
| $\beta$ | Rail incline angle. |
| $z_V, z_{Bi}$ | Vehicle body & bogie vertical displacements. |
| $F_{Pij}, F_{Sij}$ | Vertical primary & secondary suspension forces. |
| $F_{MBij}$ | Forces from the motor housings to the bogies |
| $I_V, I_{Bi}$ | Vehicle body & bogies pitch moment of inertias. |
| $\theta_V, \theta_{Bi}$ | Vehicle body & bogies pitch angles. |
| $k_{Ti}, c_{Ti}, k_{Pij}, c_{Pij}$, $k_{Sij}, c_{Sij}$ | Traction rod, primary suspension vertical, & secondary suspension vertical stiffness & damping coefficients. |
| $k_{PXij}$ | Primary suspension longitudinal stiffness coefficients. |
| $I_L, I_R, I_M, I_G, I_P$ | Left wheel, right wheel, motor rotor, gear wheel and pinion moment of inertias. |
| $\theta_L, \theta_R, \theta_M, \theta_G, \theta_P$ | Respective angles. |
| $c_1, k_1, c_2, k_2, c_3, k_3$ | Damping and stiffness coefficients between the left wheel & gear wheel, right wheel & gear wheel, and the motor & pinion. |
| $r_L, r_R$ | Radii from the left and right wheel centres to the wheel-rail contact point. |
| $F_{PG}$ | Force between the gear wheel and pinion. |
| $n_G, n_P$ | Gear wheel and pinion radii. |
| $R$ | Gear ratio. |
| $F_C$ | Coupler force. |
| $x_W$ | Wagons longitudinal position. |
| $c_C, k_C$ | Coupler damping and stiffness coefficients. |

Other than the normal force calculation, the simulation model remains mostly unchanged from Van de Merwe and Le Roux (2022). Table 1 describes the parameters used in these sections. The subscripts $ij$ indicate the front, $i = 1$, or rear, $i = 2$ bogies, and the front, $j = 1$, or rear, $j = 2$ wheelsets of that bogie. The $H$ and $L$ parameters are the geometric heights and lengths, as indicated in the figures.

### 2.1. Longitudinal, vertical and pitch dynamics

The locomotive longitudinal dynamics are determined by Newton's Second Law and are given by:

$$m_V \ddot{x}_V = F_{T1} + F_{T2} - F_C \cos\theta_V - F_{gV} \sin\beta \tag{3a}$$

$$m_{Bi} \ddot{x}_{Bi} = F_{PXi1} + F_{PXi2} - F_{Ti} - F_{gBi} \sin\beta \tag{3b}$$

$$m_{Wij} \ddot{x}_{Wij} = F_{aLij} + F_{aRij} - F_{PXij} - F_{gWij} \sin\beta. \tag{3c}$$

Similarly, the vertical dynamics are:

$$m_V \ddot{z}_V = -F_{S11} - F_{S12} - F_{S21} - F_{S22} - F_C \sin\theta_V + F_{gV} \cos\beta \tag{4a}$$

$$m_{Bi} \ddot{z}_{Bi} = -F_{Pi1} - F_{Pi2} - F_{MBi1} - F_{MBi2} + F_{Si1} + F_{Si2} + F_{gBi} \cos\beta. \tag{4b}$$

The pitch dynamics are determined by a moment balance and are described by:

$$\begin{aligned} I_V \ddot{\theta}_V = {} & L_{V11} F_{S11} + L_{V12} F_{S12} - L_{V21} F_{S21} - L_{V22} F_{S22} \\ & + H_{VT} F_{T1} + H_{VT} F_{T2} - H_C F_C \cos\theta_V - L_C F_C \sin\theta_V \end{aligned} \tag{5a}$$

$$\begin{aligned} I_{Bi} \ddot{\theta}_{Bi} = {} & L_{Pi1} F_{Pi1} - L_{Pi2} F_{Pi2} - L_{Si1} F_{Si1} + L_{Si2} F_{Si2} + L_{MBi1} F_{MBi1} \\ & - L_{MBi2} F_{MBi2} + H_P (F_{PXi1} + F_{PXi2}) + H_{BT} F_{Ti}. \end{aligned} \tag{5b}$$

### 2.2. Suspension forces

The longitudinal suspension forces in Fig. 4 are:

$$F_{Ti} = k_{Ti}(x_{Bi} - x_V) + c_{Ti}(\dot{x}_{Bi} - \dot{x}_V) \tag{6a}$$

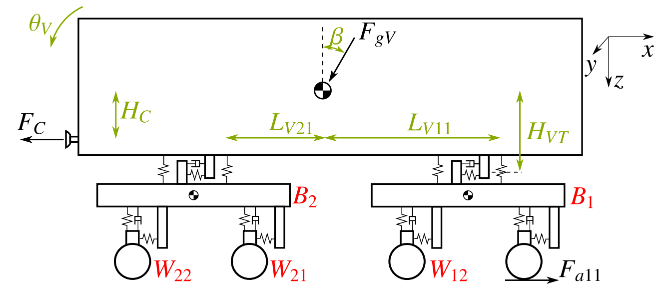


**Fig. 3.** Locomotive model. Front ($B_1$) and rear ($B_2$) bogies, with the front ($W_{i1}$) and rear ($W_{i2}$) wheelsets.

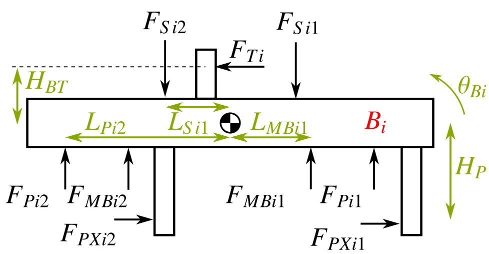


**Fig. 4.** Forces acting on a bogie.

$$F_{PXij} = k_{PXij}(x_{Wij} - x_{Bi}). \tag{6b}$$

The vertical primary suspension forces are:

$$F_{Pij} = k_{Pij}(z_{Bi} \mp L_{Pij}\theta_{Bi}) + c_{Pij}(\dot{z}_{Bi} \mp L_{Pij}\dot{\theta}_{Bi}). \tag{7}$$

The signs are negative for the front wheelsets and positive for the rear wheelsets of each bogie. The secondary suspension forces are:

$$\begin{aligned} F_{Sij} &= k_{Sij}(z_V - z_{Bi} \mp L_{Vij}\theta_V \pm L_{Sij}\theta_{Bi}) \\ &\quad + c_{Sij}(\dot{z}_V - \dot{z}_{Bi} \mp L_{Vij}\dot{\theta}_V \pm L_{Sij}\dot{\theta}_{Bi}). \end{aligned} \tag{8}$$

The signs preceding the $L_{Vij}$ terms are negative for the front bogie and positive for the rear bogie. The signs preceding the $L_{Sij}$ terms are positive for the front wheelsets and negative for the rear wheelsets of each bogie.

### 2.3. Wheelset rotational dynamics

The wheelset model is illustrated in Fig. 5. The wheelset rotational dynamics are:

$$I_L\ddot{\theta}_L = -r_L F_{aL} + c_1(\dot{\theta}_G - \dot{\theta}_L) + k_1(\theta_G - \theta_L) \tag{9a}$$

$$I_R\ddot{\theta}_R = -r_R F_{aR} + c_2(\dot{\theta}_G - \dot{\theta}_R) + k_2(\theta_G - \theta_R) \tag{9b}$$

$$I_M\ddot{\theta}_M = T_M + c_3(R\dot{\theta}_G - \dot{\theta}_M) + k_3(R\theta_G - \theta_M) \tag{9c}$$

$$\begin{aligned} I_G\ddot{\theta}_G &= n_G F_{PG} + c_1(\dot{\theta}_L - \dot{\theta}_G) + k_1(\theta_L - \theta_G) \\ &\quad + c_2(\dot{\theta}_R - \dot{\theta}_G) + k_2(\theta_R - \theta_G) \end{aligned} \tag{9d}$$

$$I_P\ddot{\theta}_P = -n_P F_{PG} + c_3(\dot{\theta}_M - \dot{\theta}_P) + k_3(\theta_M - \theta_P), \tag{9e}$$

with:

$$R = \frac{n_G}{n_P} = \frac{\theta_G}{\theta_P}. \tag{10}$$

By substituting $F_{PG}$ from (9e) into (9d) and using (10):

$$\begin{aligned} &(I_G + R^2 I_P)\ddot{\theta}_G + (c_1 + c_2 + R^2 c_3)\dot{\theta}_G + (k_1 + k_2 + R^2 k_3)\theta_G - c_1\dot{\theta}_L \\ &- c_2\dot{\theta}_R - Rc_3\dot{\theta}_M - k_1\theta_L - k_2\theta_R - Rk_3\theta_M = 0. \end{aligned} \tag{11}$$

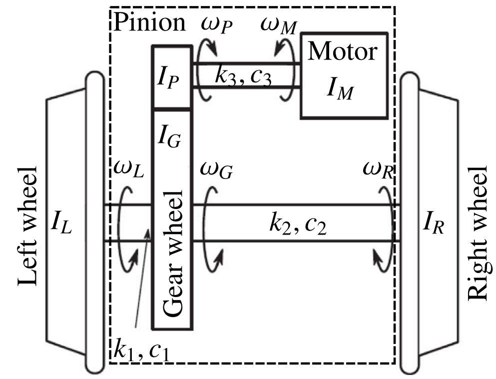


**Fig. 5.** Wheelset model (bottom view). The dashed line represents the motor housing in Fig. A.21.

### 2.4. Interface/external forces

A spring and damper element simulates the coupler's connection between the locomotive and the wagons, so that the coupler force is:

$$F_C = k_C(x_V - x_W) + c_C(\dot{x}_V - \dot{x}_W). \tag{12}$$

A single axle wheelset model is used to model the wagons, as described in Ararat and Söylemez (2017) and Ohishi et al. (1998). This modelling approach lumps the inertia of the wheelsets of the wagon together, has the same mass as the wagons, and aggregates the adhesion forces of each wheel to define the adhesion force for this composite model.

The Polach model (Polach, 2005) is used to calculate the adhesion forces and is described in Section 3. To calculate the adhesion force of a wheel (the adhesion force of each wheel is calculated separately), the surface velocity, the locomotive velocity, and the wheel-rail normal force are required. The normal forces of the simulation model in Van de Merwe and Le Roux (2022) considered only the wheelset gravitational and primary suspension forces. However, the normal forces can be modelled more accurately by considering the variation caused by the motor torques, as presented in Appendix A.

The desired motor torque calculation is given in Appendix B.

### 2.5. Consolidated simulation model

Mass, damping, and stiffness matrices, $\boldsymbol{M}_q$, $\boldsymbol{C}_q$ and $\boldsymbol{K}_q$, are constructed from the longitudinal (3), vertical (4), pitch (5) and wheelset rotational dynamics (9) & (11), so that (Spiryagin et al., 2017):

$$\boldsymbol{M}_q\ddot{\boldsymbol{q}} + \boldsymbol{C}_q\dot{\boldsymbol{q}} + \boldsymbol{K}_q\boldsymbol{q} = \boldsymbol{f}. \tag{13}$$

The displacement vector is (with dimension given in brackets):

$$\begin{aligned} \boldsymbol{q}_{(29\times1)} = \big[ & x_V \quad x_{B1} \quad x_{W11} \quad x_{W12} \quad x_{B2} \quad x_{W21} \quad x_{W22} \quad z_V \\ & \dots\ z_{B1} \quad z_{B2} \quad \theta_V \quad \theta_{B1} \quad \theta_{B2} \quad \theta_{L11} \quad \theta_{R11} \quad \theta_{G11} \\ & \dots\ \theta_{M11} \quad \theta_{L12} \quad \theta_{R12} \quad \theta_{G12} \quad \theta_{M12} \quad \theta_{L21} \quad \theta_{R21} \\ & \dots\ \theta_{G21} \quad \theta_{M21} \quad \theta_{L22} \quad \theta_{R22} \quad \theta_{G22} \quad \theta_{M22} \big]^T. \end{aligned} \tag{14}$$

The interface force vector, $\boldsymbol{f}$, contains the gravitational forces, adhesion forces, coupler force, motor torques, and motor housing to bogie forces. Detailed formulae for the vectors and matrices in (13) are given in Van de Merwe (2023). By choosing the state vector as:

$$\boldsymbol{x} = \begin{bmatrix} \boldsymbol{q} \\ \dot{\boldsymbol{q}} \end{bmatrix}, \tag{15}$$

the state-space form can be constructed:

$$\dot{\boldsymbol{x}} = \boldsymbol{A}\boldsymbol{x} + \boldsymbol{B}\boldsymbol{f}, \tag{16}$$

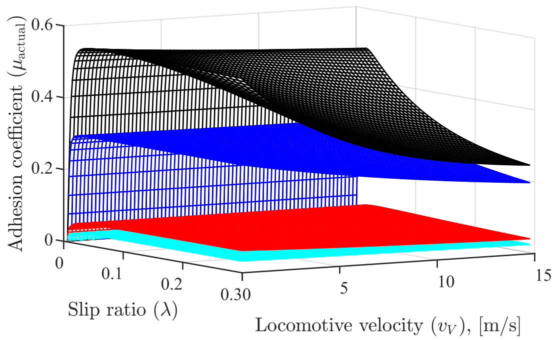


**Fig. 6.** Actual adhesion in *dry* (black), *wet* (blue), *low* (red), and *very low* (cyan) adhesion conditions. (For interpretation of the references to colour in this figure legend, the reader is referred to the web version of this article.)

with:

$$A = \begin{bmatrix} \mathbf{0} & \mathbf{I} \\ -\mathbf{M}_q^{-1}\mathbf{K}_q & -\mathbf{M}_q^{-1}\mathbf{C}_q \end{bmatrix}, \quad \mathbf{B} = \begin{bmatrix} \mathbf{0} \\ \mathbf{M}_q^{-1} \end{bmatrix}. \tag{17}$$

## 3. Wheel-rail contact dynamics

The adhesion forces are computed from the wheel-rail contact dynamics, described by Burckhardt's simplified model (He et al., 2018), the LuGre model (Ararat & Söylemez, 2017; Kayacan et al., 2009; Kun et al., 2006) or the Polach model (Polach, 2005). These models agree on the curve shape but differ in the maximum adhesion location (Pichlik, 2019).

The Polach model is most commonly used to calculate the adhesion force in rail applications (Wang et al., 2019) since it is a railway-specific model verified through extensive experiments (Ararat & Söylemez, 2017). This model assumes that the initial creep curve has a varying slope for different adhesion conditions and models the non-linear adhesion characteristics beyond the creep saturation (Ward et al., 2011). The Polach model can be described as shown below (Charles et al., 2008; Spiryagin et al., 2011; Wang et al., 2019).

The adhesion coefficient $\mu$ is:

$$\mu = \mu_0\left((1-A)e^{-Bv_s} + A\right) \tag{18}$$

$$A = \frac{\mu_\infty}{\mu_0}, \tag{19}$$

where $v_s = r\omega_d - v_V$ is the slip velocity, $A$ is the ratio of friction coefficients, $\mu_0$ is the maximum friction coefficient at zero slip, $\mu_\infty$ is the maximum friction coefficient at infinity slip, and $B$ is the coefficient of exponential friction decrease. The adhesion force is:

$$F_a = \frac{2\mu F_N}{\pi}\left(\frac{k_A\epsilon}{1+(k_A\epsilon)^2} + \arctan(k_S\,\epsilon)\right), \tag{20}$$

with:

$$\epsilon = \frac{G\pi abC_1}{4F_N\mu}\lambda, \tag{21}$$

where $F_N$ is the normal force, $\lambda$ is the slip ratio, $k_A$ and $k_S$ are reduction factors in the adhesion area, and $\epsilon$ is the gradient of the tangential stress in the adhesion area, $G$ is the shear module, $a$ and $b$ are the lengths of the semi-axis of the elliptic contact patch respectively, and $C_1$ is the Kalker's linear creep theory coefficient (Kalker, 1990).

By defining the adhesion force as the product of the actual (or realized) adhesion and the force between the wheel and rail, i.e. $F_a = \mu_{\text{actual}}F_N$, then from (20):

$$\mu_{\text{actual}} = \frac{2\mu}{\pi}\left(\frac{k_A\epsilon}{1+(k_A\epsilon)^2} + \arctan(k_S\,\epsilon)\right). \tag{22}$$

This function is plotted in Fig. 6 for different adhesion levels. The *low* and *very low* conditions can be a result of contaminants such as oil or compressed leaves (Hubbard et al., 2016). Whenever the adhesion coefficient is referred to in the rest of this paper, it refers to the actual adhesion coefficient, $\mu_{\text{actual}}$.

## 4. Estimator

As indicated in Fig. 2, the wheel-slip controller and the reference adaptation require estimates of the slip ratio, locomotive velocity, adhesion coefficient, and normal force. Computing these estimates is described in this section.

### 4.1. Adhesion force estimation model

Typically, the motor's angular rate is measured with an encoder, and its torque is estimated within the motor control system (Pretagostini et al., 2020). These two known parameters are insufficient for the full wheelset model in Section 2.3 to produce an observable estimator where both adhesion forces are estimated. By applying a known motor torque, a specific angular velocity response is expected based on the known system dynamics. The estimator should be able to resolve the difference between the measured angular velocity and the expected angular velocity by estimating the disturbance caused by the adhesion forces. By assuming both adhesion forces are equal, $\frac{1}{2}F_a = F_{aL} = F_{aR}$, an observable estimator can be produced. Here, the adhesion force estimate, $F_a$, represents an approximation of the combined adhesion forces of the left and right wheels. Within the context of slip control, the difference in the adhesion forces of the left and right wheels is inconsequential since they cannot be controlled independently in most applications.

#### 4.1.1. Wheelset model

The wheelset state-space model is:

$$\dot{\mathbf{x}}_w = \mathbf{A}_w\mathbf{x}_w + \mathbf{B}_w\mathbf{f}_w \tag{23a}$$

$$\mathbf{y}_w = \mathbf{C}_w\mathbf{x}_w, \tag{23b}$$

where (23a) is derived from (9) and (11) using (13) to (17) by selecting the displacement vector as:

$$\mathbf{q}_w = \begin{bmatrix}\theta_L & \theta_R & \theta_G & \theta_M\end{bmatrix}^T. \tag{24}$$

The interface force vector is:

$$\mathbf{f}_w = \begin{bmatrix} -r_L F_{aL} \\ -r_R F_{aR} \\ 0 \\ T_M \end{bmatrix}. \tag{25}$$

The outputs relevant to the estimator are the motor angular velocity, $\omega_M = \dot{\theta}_M$, and the left (or right) wheel surface velocity, $v_{dL} = r_L\omega_L$ (where $\omega_L = \dot{\theta}_L$). Therefore, the output matrix is:

$$\mathbf{C}_w = \begin{bmatrix} 0 & 0 & 0 & 0 & 0 & 0 & 0 & 1 \\ 0 & 0 & 0 & 0 & r_L & 0 & 0 & 0 \end{bmatrix}. \tag{26}$$

The model of (23) contains three complex pole pairs due to the three non-rigid axles of the wheelset and two integrators. Since both relevant outputs are velocities, one of the integrators will produce an unobservable and uncontrollable mode (the absolute angles cannot be determined). Therefore, a minimum realization reduces the order of the model from eight to seven:

$$\tilde{\mathbf{G}}_{\min}(s) \overset{s}{=} \left[\begin{array}{c|c} \mathbf{A}_{\min} & \mathbf{B}_{\min} \\ \hline \mathbf{C}_{\min} & [0]_{2\times4} \end{array}\right] \overset{s}{=} \text{minreal}\left[\begin{array}{c|c} \mathbf{A}_w & \mathbf{B}_w \\ \hline \mathbf{C}_w & [0]_{2\times4} \end{array}\right]. \tag{27}$$

The tilde symbol indicates that the plant is not scaled (input–output normalized), minreal is the minimum realization function, and $[0]_{p\times q}$ is a matrix of zeros with $p$ rows and $q$ columns. This model can be simplified further using a balanced truncation to maintain the most significant frequency components, as outlined in Skogestad and Postlethwaite (2005).

#### 4.1.2. Model order reduction

A balanced realization can only be produced from a given realization if it is asymptotically stable (Green & Limebeer, 2012). Therefore, the integrator should be separated from the model before reduction of the stable part. An orthogonal matrix, $\boldsymbol{Q}$, can be found[1] that transforms $\boldsymbol{A}_{\text{min}}$ to the upper Schur form:

$$\boldsymbol{Q}\boldsymbol{A}_{\text{min}}\boldsymbol{Q}^T = \begin{bmatrix} \boldsymbol{A}_{11} & \boldsymbol{A}_{12} \\ \boldsymbol{0} & \boldsymbol{A}_{22} \end{bmatrix}, \tag{28}$$

so that $\text{Re}(\lambda_i(\boldsymbol{A}_{11})) < 0$ and $\text{Re}(\lambda_i(\boldsymbol{A}_{22})) \geq 0$ (Glover, 1984), where $\boldsymbol{Q}^T$ is the transpose of $\boldsymbol{Q}$ and $\lambda_i$ here indicates the $i'$th eigenvalue. For this case $\boldsymbol{A}_{22}$ will be a scalar containing the integrator, i.e. $A_{22} = 0$. A second transformation is performed so that:

$$\begin{bmatrix} \boldsymbol{I} & -\boldsymbol{X} \\ \boldsymbol{0} & \boldsymbol{I} \end{bmatrix} \begin{bmatrix} \boldsymbol{A}_{11} & \boldsymbol{A}_{12} \\ \boldsymbol{0} & \boldsymbol{A}_{22} \end{bmatrix} \begin{bmatrix} \boldsymbol{I} & \boldsymbol{X} \\ \boldsymbol{0} & \boldsymbol{I} \end{bmatrix} = \begin{bmatrix} \boldsymbol{A}_{11} & \boldsymbol{A}_{11}\boldsymbol{X} - \boldsymbol{X}\boldsymbol{A}_{22} + \boldsymbol{A}_{12} \\ \boldsymbol{0} & \boldsymbol{A}_{22} \end{bmatrix}, \tag{29}$$

where $\boldsymbol{X}$ is the solution of $\boldsymbol{A}_{11}\boldsymbol{X} - \boldsymbol{X}\boldsymbol{A}_{22} + \boldsymbol{A}_{12} = \boldsymbol{0}$ (Glover, 1984). In this case $A_{22} = 0$; therefore: $\boldsymbol{X} = -\boldsymbol{A}_{11}^{-1}\boldsymbol{A}_{12}$.

The new state space matrices are:

$$\begin{aligned} \bar{\boldsymbol{A}}_{(7\times7)} &= \boldsymbol{T}\boldsymbol{Q}\boldsymbol{A}_{\text{min}}\boldsymbol{Q}^T\boldsymbol{T}^{-1} = \begin{bmatrix} \boldsymbol{A}_{11} & \boldsymbol{0} \\ \boldsymbol{0} & A_{22} \end{bmatrix} \\ \bar{\boldsymbol{B}}_{(7\times4)} &= \boldsymbol{T}\boldsymbol{Q}\boldsymbol{B}_{\text{min}} = \begin{bmatrix} \bar{\boldsymbol{B}}_1 \\ \bar{B}_2 \end{bmatrix} \\ \bar{\boldsymbol{C}}_{(2\times7)} &= \boldsymbol{C}_{\text{min}}\boldsymbol{Q}^T\boldsymbol{T}^{-1} = \begin{bmatrix} \bar{\boldsymbol{C}}_1 & \bar{C}_2 \end{bmatrix}, \end{aligned} \tag{30}$$

where $\boldsymbol{T} = \begin{bmatrix} \boldsymbol{I} & -\boldsymbol{X} \\ \boldsymbol{0} & \boldsymbol{I} \end{bmatrix}$, and the sizes of the matrices are given in brackets for clarity. The desired model is constructed from the Section of this new state space model without the integrator:

$$\tilde{\boldsymbol{G}}_{\text{sec}} \stackrel{s}{=} \left[ \begin{array}{c|c} \boldsymbol{A}_{11} & \bar{\boldsymbol{B}}_1 \\ \hline \bar{\boldsymbol{C}}_1 & [0]_{2\times4} \end{array} \right]. \tag{31}$$

The Hankel singular values of $\tilde{\boldsymbol{G}}_{\text{sec}}$ are: $\sigma_i = [11.4 \times 10^{-3},\ 11.4 \times 10^{-3},\ 6.7 \times 10^{-3},\ 6.7 \times 10^{-3},\ 95.6 \times 10^{-6},\ 95.6 \times 10^{-6}]$. The last two singular values are much smaller than the others, which indicates that the order of this model can be reduced to four without impacting the input–output behaviour significantly. The intermediate reduced order model is:

$$\tilde{\boldsymbol{G}}_{\text{int}}(s) \stackrel{s}{=} \left[ \begin{array}{c|c} \boldsymbol{A}_{\text{int}} & \boldsymbol{B}_{\text{int}} \\ \hline \boldsymbol{C}_{\text{int}} & [0]_{2\times4} \end{array} \right] \stackrel{s}{=} \text{balred}\{\tilde{\boldsymbol{G}}_{\text{sec}}\}. \tag{32}$$

where balred is the balanced order reduction function with the order specified as four. The $\mathcal{H}^\infty$ error caused by this truncation, $\|\tilde{\boldsymbol{G}}_{\text{sec}} - \tilde{\boldsymbol{G}}_{\text{int}}\|_\infty$, will be less than or equal to $2(95.6e^{-6} + 95.6e^{-6}) = 382.4e^{-6}$ (Green & Limebeer, 2012). The integrator is added back to (32) to produce the reduced order model:

$$\begin{aligned} \boldsymbol{A}_{\text{red}} &= \begin{bmatrix} \boldsymbol{A}_{\text{int}} & [0]_{4\times1} \\ [0]_{1\times4} & A_{22} \end{bmatrix} \quad \boldsymbol{B}_{\text{red}} = \begin{bmatrix} \boldsymbol{B}_{\text{int}} \\ \bar{B}_2 \end{bmatrix} \\ \boldsymbol{C}_{\text{red}} &= \begin{bmatrix} \boldsymbol{C}_{\text{int}} & \bar{C}_2 \end{bmatrix}, \end{aligned} \tag{33}$$

By comparing the frequency responses of the motor torque, $T_M$, to motor angular velocity, $\omega_M$, of the minimum realization model in (27) and the reduced order model in (33) in Fig. 7, it is shown that the reduced order model preserves the two largest resonant peaks and the peak caused by the high-frequency complex pole-zero pairs is removed.

In terms of the model parameters to produce Fig. 7, wheelset inertias were obtained from a CAD-based mass property analysis. Stiffness and damping parameters were calibrated to ensure that resonant peak frequencies align with experimental data in Reitmann (2017). Torsional vibrations are primarily excited by negative damping in the wheel–rail contact patch during unstable slip. These vibrations are especially pronounced under asymmetric adhesion conditions between the left and right wheels, which generate a moment in the axle that excites its torsional modes—resonances that occur at the identified peak frequencies (Reitmann, 2017). An exaggerated asymmetry between the wheels was introduced, $k_2 = 0.7\,k_1$, to promote torsional vibrations observed in practice.

[1] See MATLAB's schur function.

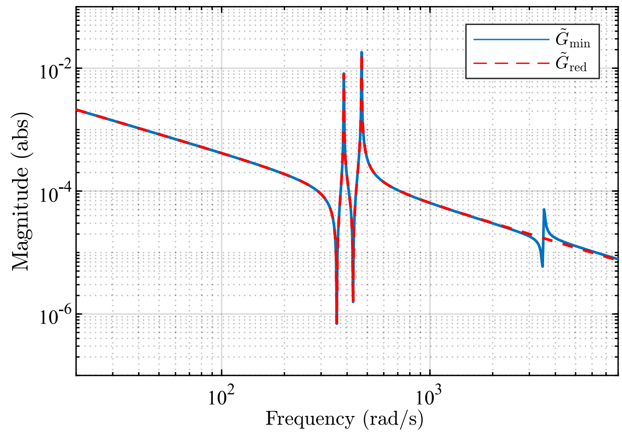


**Fig. 7.** Bode plot of the motor torque, $T_M$, to motor angular velocity, $\omega_M$, for the minimum realization and reduced order models.

#### 4.1.3. Estimation model

An estimator can be constructed from the model in (33) by modelling the adhesion force as random walks, i.e. $\dot{F}_a = 0$ (Ward et al., 2012). The input to the estimator is the motor torque, $u_{\text{est}} = T_M$, and the measured output is the motor angular velocity, $y_{\text{est}} = \omega_M$. Therefore, the state vector of the estimator is:

$$\boldsymbol{x}_{\text{est}} = \begin{bmatrix} \boldsymbol{x}_{\text{red}} \\ F_a \end{bmatrix}, \tag{34}$$

where $\boldsymbol{x}_{\text{red}}$ is the state vector (five states) of the model in (33), and state-space matrices of the estimator are:

$$\boldsymbol{A}_{\text{est}\,(6\times6)} = \begin{bmatrix} \boldsymbol{A}_{\text{red}} & \frac{1}{2}(-r_L \cdot \boldsymbol{B}_{\text{red}[:,1]} - r_R \cdot \boldsymbol{B}_{\text{red}[:,2]}) \\ [0]_{1\times5} & 0 \end{bmatrix} \tag{35a}$$

$$\boldsymbol{B}_{\text{est}\,(6\times1)} = \begin{bmatrix} \boldsymbol{B}_{\text{red}[:,4]} \\ 0 \end{bmatrix} \tag{35b}$$

$$\boldsymbol{C}_{\text{est}\,(1\times6)} = \begin{bmatrix} \boldsymbol{C}_{\text{red}[1,:]} & 0 \end{bmatrix} \tag{35c}$$

$$D_{\text{est}} = 0, \tag{35d}$$

where $\boldsymbol{X}_{[a,:]}$ and $\boldsymbol{X}_{[:,b]}$ is the $a$ row and $b$ column vectors of matrix $\boldsymbol{X}$ respectively.

The sixth state in (34) contains the estimate of the adhesion force. The estimates of the motor angular velocity and the left wheel surface velocity are obtained by:

$$\hat{\omega}_M = \boldsymbol{C}_{\text{red}[1,:]}\hat{\boldsymbol{x}}_{\text{red}} \tag{36}$$

$$\hat{v}_{dL} = \boldsymbol{C}_{\text{red}[2,:]}\hat{\boldsymbol{x}}_{\text{red}}, \tag{37}$$

where $\hat{\boldsymbol{x}}_{\text{red}}$ is the estimates of the first five states of (34), produced by a Kalman filter.

### 4.2. Longitudinal dynamics estimation model

As discussed in Van de Merwe and Le Roux (2023), accurate locomotive velocity and acceleration estimates can be produced in a Kalman filter that includes the longitudinal dynamics of the locomotive, where the acceleration and velocity are measured using an inertial measurement unit (IMU) and a Doppler radar respectively. In Van de

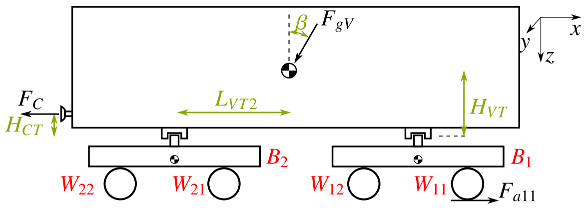


**Fig. 8.** Pitch-plane of the locomotive. (Front ($B_1$) and rear ($B_2$) bogie and the front ($W_{i1}$) and rear ($W_{i2}$) wheelset of each bogie indicated.)

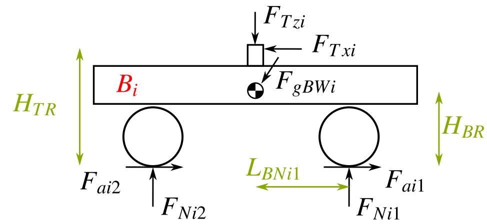


**Fig. 9.** A single bogie of the locomotive body. (Front ($B_1$) and rear ($B_2$) bogie and the front ($W_{i1}$) and rear ($W_{i2}$) wheelset of each bogie indicated.)

Merwe and Le Roux (2023), a simplified model as shown in Fig. 8 is used to model the longitudinal dynamics, which are repeated here:

$$m_L \dot{v}_V = F_{a11} + F_{a12} + F_{a21} + F_{a22} - F_C - F_{gL} \sin\beta. \tag{38}$$

Here $m_L$ is the total locomotive weight, $F_{aij}$ are the adhesion forces, and $F_{gL} = m_L g$ is the gravitational force of the locomotive. This model does not include the full train longitudinal dynamics, and the coupler force, $F_C$, is modelled as an unknown disturbance acting on the coupler, thereby making the estimation approach agnostic to variations in wagon loading (Van de Merwe & Le Roux, 2023). The rail angle, $\beta$, is determined by low-pass filtering the locomotive body angle measurement computed using the IMU. As demonstrated in the subsequent subsection, this model can be integrated with the reduced-order wheelset model for each individual wheelset. This yields a state-observable model capable of generating the desired estimates.

### 4.3. Kalman-Bucy filter

No assumptions are made about the nonlinear contact dynamics, which are subject to frequent variation in practice. Consequently, the estimation model is linear, and the use of a linear Kalman filter is justified (cf. Charles et al. (2008) and Ward et al. (2011)).

As done in Van de Merwe and Le Roux (2022), the longitudinal and reduced order wheelset models are combined in a single state space system by choosing the state vector as:

$$\boldsymbol{x} = \begin{bmatrix} v_V & F_{a11} & F_{a12} & F_{a21} & F_{a22} & F_C \\ \dots & \boldsymbol{x}_{\text{red}11}^T & \boldsymbol{x}_{\text{red}12}^T & \boldsymbol{x}_{\text{red}21}^T & \boldsymbol{x}_{\text{red}22}^T \end{bmatrix}^T, \tag{39}$$

the interface force vector as:

$$\boldsymbol{f} = \begin{bmatrix} -F_{gL}\sin\beta & T_{M11} & T_{M12} & T_{M21} & T_{M22} \end{bmatrix}^T, \tag{40}$$

and by modelling the unknown forces as random walks by setting $\dot{F}_{a11} = \dot{F}_{a12} = \dot{F}_{a21} = \dot{F}_{a22} = \dot{F}_C = 0$ (Ward et al., 2012). The measured outputs are:

$$\boldsymbol{y} = \begin{bmatrix} \dot{v}_V & v_V & \omega_{M11} & \omega_{M12} & \omega_{M21} & \omega_{M22} \end{bmatrix}^T. \tag{41}$$

A Kalman-Bucy filter is described by:

$$\dot{\hat{\boldsymbol{x}}} = \boldsymbol{A}\hat{\boldsymbol{x}} + \boldsymbol{B}\boldsymbol{f} + \boldsymbol{K}(\boldsymbol{y} - \hat{\boldsymbol{y}}) \tag{42a}$$

$$\hat{\boldsymbol{y}} = \boldsymbol{C}\hat{\boldsymbol{x}}, \tag{42b}$$

where $\hat{\boldsymbol{x}}$ and $\hat{\boldsymbol{y}}$ are the estimated states and outputs, $\boldsymbol{y}$ is the measured outputs, and $\boldsymbol{K}$ is the Kalman gain (Grewal & Andrews, 2015; Ward et al., 2012). The Kalman gain is given by:

$$\boldsymbol{K} = \boldsymbol{P}\boldsymbol{C}^T\boldsymbol{R}^{-1} \tag{43a}$$

$$\dot{\boldsymbol{P}} = \boldsymbol{A}\boldsymbol{P} + \boldsymbol{P}\boldsymbol{A}^T - \boldsymbol{K}\boldsymbol{R}\boldsymbol{K}^T + \boldsymbol{Q}, \tag{43b}$$

where $\boldsymbol{P}$ is the error covariance matrix. The process noise covariance matrix, $\boldsymbol{Q}$, is chosen as:

$$\boldsymbol{Q} = \text{diag}[10,\ [1\times 10^{12}]_{1\times 5},\ [1]_{1\times 20}], \tag{44}$$

which attributes large uncertainty to the assumption that $\dot{F}_{aij} = 0$ and $\dot{F}_C = 0$ (rows 2 to 6 in (42a)) (Ward et al., 2012). In other words, the high gains treat these forces as unknown inputs, enabling the filter to adapt more readily to real-world variability. The measurement noise covariance matrix, $\boldsymbol{R}$, is set to:

$$\boldsymbol{R} = \text{diag}[5,\ 10,\ [1]_{1\times 4}], \tag{45}$$

because the encoder measurements are expected to have lower noise than the longitudinal acceleration and velocity measurements. The chosen $\boldsymbol{Q}$ and $\boldsymbol{R}$ are time-invariant. Therefore, $\dot{\boldsymbol{P}} = 0$ and (43b) becomes the well known algebraic Riccati equation (Ward et al., 2012). Solving this algebraic equation gives a constant Kalman gain $\boldsymbol{K}$.

### 4.4. Normal force estimate

A pitch-plane model can be used to calculate the normal force distribution between the wheelsets. Afterwards, the left and right wheel normal forces can be calculated with a roll plane model (Rezaeian et al., 2015). Considering that the difference between the left and right wheel adhesion forces is not of interest here, as mentioned in Section 4.1, calculating the difference between the left and right normal forces is unnecessary. The derivation of the wheelset normal forces are given in Van de Merwe and Le Roux (2023), and the results are summarized here. The normal forces are:

$$F_{Nij} = \frac{1}{(L_{BNi1} + L_{BNi2})}[\mp H_{BR} m_{BWi} a_V \mp H_{TR} F_{Txi} \\ + L_{BNi2}(F_{Tzi} + m_{BWi} g\cos\beta) \mp H_{BR} m_{BWi} g \sin\beta], \tag{46}$$

where the signs are negative for the front wheelsets and positive for the rear wheelsets. Here $m_{BWi}$ is the weight of the bogie. The geometric heights and lengths are indicated in Figs. 8 & 9. The vertical force between the bogies and the body, $F_{Tzi}$, as shown in Fig. 9, are:

$$F_{Tzi} = \frac{1}{L_{VT1} + L_{VT2}}[\mp H_{VT} m_V a_V \mp H_{CT} F_C \\ \mp H_{VT} m_V g\sin\beta + L_{VT_i} m_V g\cos\beta], \tag{47}$$

where the signs are negative for the front bogie and positive for the rear bogie. The longitudinal forces between the body and bogies, $F_{Txi}$, as shown in Fig. 9, are:

$$F_{Txi} = F_{ai1} + F_{ai2} - m_{BWi}(a_V + g\sin\beta). \tag{48}$$

The normal forces are calculated from the estimates produced by the estimator in Section 4.3, namely the acceleration, $\hat{a}_v = \dot{\hat{x}}_1$, adhesion forces, and the coupler force. The presented strategy to estimate the normal forces cannot be used directly on a Co-Co locomotive (three wheelsets per bogie). In that case, a feasible approach is to assume a linear distribution of the normal forces across the wheelsets within a bogie.

### 4.5. Adhesion coefficient and slip ratio estimation

The adhesion coefficients and slip ratio estimates of each wheelset are given by (Van de Merwe & Le Roux, 2023):

$$\hat{\mu}_{ij} = \hat{F}_{aij}/\hat{F}_{Nij} \tag{49}$$

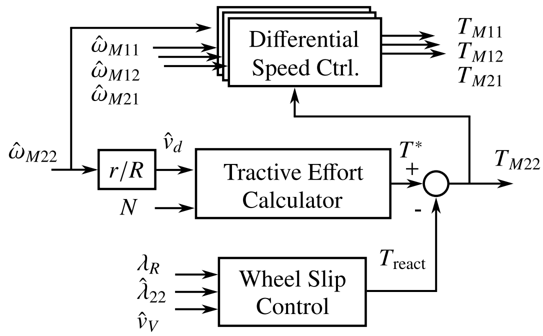


**Fig. 10.** Slip control structure (cf. Fig. 2) where the rear wheelset is controlled by the *Wheel Slip Control* block (see Fig. 13). The torque and speed of the rear wheelset are used as references for the remaining wheelsets which are controlled by parallel Differential Speed Controllers (see Fig. 11).

$$\hat{\lambda}_{ij} = \pm(\hat{v}_{dLij} - \hat{v}_V)/\hat{v}_V, \tag{50}$$

where $\hat{v}_{dLij}$ is calculated from (37), the adhesion force estimates and the locomotive velocity estimate are provided from the Kalman-Bucy filter in Section 4.3, and the normal forces are calculated as outlined in Section 4.4.

A benefit of this approach is that the estimates are produced from a linear model since none of the non-linear contact dynamics are included in the model, and the adhesion forces are assumed to be unknown.

However, a limitation of this estimation approach pertains to its assumption of constant wheel radii, which could impact the performance of the estimator when the locomotive travels along a curve. An alternative, albeit intricate, strategy involves incorporating the radii as dynamic states to be estimated (Charles et al., 2006, 2008). The favoured method treats radii variations as uncertainties and ensures that the reference adaptation and slip control system are sufficiently robust to accommodate such uncertainties (Berntorp, 2016).

## 5. Slip control

When the locomotive is accelerating, the weight redistribution causes a decrease in the normal force of the front wheelsets and an increase in the rear wheelsets. The front wheelset (with the smallest normal force) is the most likely to slip. If slip can be prevented in the rear wheelset, i.e., $W_{22}$, its torque and speed ($T_{M22}$ and $\hat{\omega}_{M22}$) can be used as a reference to the other wheelsets, thereby reducing the torque if they slip as shown in Fig. 10 (Yasuoka et al., 2009). Fig. 10 expands on Fig. 2 by providing a more detailed depiction of the slip control structure. To prevent slip in the rear wheelset, $W_{22}$, a PI slip controller is implemented to calculate how much the desired torque, $T^*$, should be reduced to suppress unstable slip. The PI controller is represented by the *Wheel Slip Control* block in Fig. 10 (cf. Fig. 2) and described in Section 5.3. The differential speed controllers implemented on the remaining wheelsets, i.e., $W_{11}$, $W_{12}$, and $W_{21}$, are described in Section 5.2. The complete set of controller parameters are available in Van de Merwe (2023).

### 5.1. Plant scaling

For controller design, converting the state-space system to a single input single output transfer function of the following shape is useful:

$$\tilde{y}(s) = \tilde{G}(s)\tilde{u}(s) + \tilde{G}_d(s)\tilde{d}(s). \tag{51}$$

where $y$ is the output, $G$ is the plant transfer function, $u$ is the input, $G_d$ is the disturbance transfer function, and $d$ is the disturbance input. The tilde symbol indicates that the variables and transfer functions are unscaled. The motor angular velocity is chosen as the output, $\tilde{y} = \omega_M$, the input is the motor torque, $\tilde{u} = T_M$, and by assuming the left and right adhesion forces are equal, the disturbance is: $\tilde{d} = F_a = 2F_{aL} = 2F_{aR}$. Therefore, the input and output matrices are:

$$\boldsymbol{B}_G = \boldsymbol{B}_w \begin{bmatrix} 0 & 0 & 0 & 1 \end{bmatrix}^T \tag{52}$$

$$\boldsymbol{B}_{G_d} = \boldsymbol{B}_w \begin{bmatrix} -\frac{1}{2}r_L & -\frac{1}{2}r_R & 0 & 0 \end{bmatrix}^T \tag{53}$$

$$\boldsymbol{C}_{\omega_M} = \begin{bmatrix} 0 & 0 & 0 & 0 & 0 & 0 & 0 & 1 \end{bmatrix}, \tag{54}$$

from which the transfer functions are calculated:

$$\tilde{G}_W(s) = \text{tf}\left(\text{minreal}\left[\begin{array}{c|c} \boldsymbol{A}_w & \boldsymbol{B}_G \\ \hline \boldsymbol{C}_{\omega_M} & 0 \end{array}\right]\right) \tag{55}$$

$$\tilde{G}_d(s) = \text{tf}\left(\text{minreal}\left[\begin{array}{c|c} \boldsymbol{A}_w & \boldsymbol{B}_{G_d} \\ \hline \boldsymbol{C}_{\omega_M} & 0 \end{array}\right]\right), \tag{56}$$

where $\boldsymbol{B}_w$ and $\boldsymbol{A}_w$ is defined in (23a) and tf indicates that the state-space system is converted to a transfer function.

A useful scaling for the transfer function is to make the variables less than one in magnitude (Skogestad & Postlethwaite, 2005):

$$y = \tilde{y}/\tilde{e}_{\max} = D_e^{-1}\tilde{y} \tag{57a}$$

$$u = \tilde{u}/\tilde{u}_{\max} = D_u^{-1}\tilde{u} \tag{57b}$$

$$d = \tilde{d}/\tilde{d}_{\max} = D_d^{-1}\tilde{d}, \tag{57c}$$

where $\tilde{e}_{\max}$, $\tilde{u}_{\max}$, and $\tilde{d}_{\max}$ are the maximum allowed output error, maximum input, and maximum expected disturbance respectively. The scaling factors ($D_e$, $D_u$, $D_d$) are used to scale the transfer functions:

$$G_W = D_e^{-1}\tilde{G}_W D_u \tag{58}$$

$$G_d = D_e^{-1}\tilde{G}_d D_d. \tag{59}$$

By assuming that the deflection in the axles can be ignored, the angular velocity of the motor relative to the wheel surface velocity is $\omega_M \approx R\omega_L = R\frac{v_{dL}}{r_L}$. The maximum allowed motor angular velocity error is derived by choosing the maximum allowed slip velocity, $v_s = v_{dL} - v_V$, which is chosen as 1 (m/s). The allowed error will determine the required controller bandwidth. The maximum input is the maximum torque the motor can deliver: The maximum disturbance is determined by assuming that the sum of the left and right wheel adhesion forces will not exceed 80% of the maximum tractive effort that the motor can deliver. Therefore, the scaling factors are:

$$D_e = \frac{R}{r_L} v_{s\max} \tag{60a}$$

$$D_u = T_{M\max} \tag{60b}$$

$$D_d = F_{a\max} = 0.8\,F_{t\max} = 0.8\frac{R}{r_L}T_{M\max}. \tag{60c}$$

### 5.2. Differential speed control

Differential speed controllers, as shown in Fig. 11, are implemented on wheelsets $W_{11}$, $W_{12}$ and $W_{21}$. The torque applied to the rear wheelset, $T_{M\text{ref}}$ ($T_{M22}$ in Fig. 10), is applied to the remaining wheelsets together with a feedback speed controller using the rear wheelset motor angular velocity, $\omega_{M\text{ref}}$ ($\hat{\omega}_{M22}$ in Fig. 10), as reference.

Traction motors are generally controlled using field-oriented or direct torque control, producing a fast torque response (Kim, 2017; Ronanki et al., 2017) and can be modelled simply as (Spiryagin et al., 2017):

$$G_M(s) = 1/(\tau_M s + 1), \tag{61}$$

where the time constant, $\tau_M$, is small (0.05 in this case).

As mentioned in Section 4.1, the full wheelset model has an integrator. Therefore, a simple proportional controller is sufficient. As shown in Fig. 7, the wheelset transfer function has high gains at the resonant frequencies. Torsional vibrations at these frequencies are

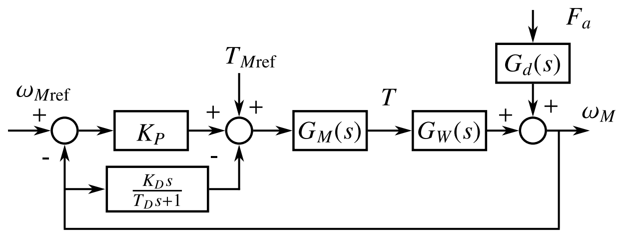


**Fig. 11.** Differential speed controller, as shown in Fig. 10, implemented individually on wheelsets $W_{11}$, $W_{12}$ and $W_{21}$.

prevalent during unstable slip. Torsional vibrations can damage the wheels and should be avoided with vibration compensation in the controller (Yasuoka et al., 2009). A feedforward derivative term is used to add damping to prevent these vibrations, as shown in Fig. 11. The required bandwidth of the controller is dependent on the disturbance transfer function $G_d$.

The reference torque, $T_{M\text{ref}}$, is not expected to vary much for slip that occurs only in the front wheelsets. Therefore, the speed controller is designed by setting $T_{M\text{ref}} = 0$. The closed loop transfer function for a feedback controller (without the feedforward derivative term) becomes:

$$y = GK(r-y) + G_d d = L(r-y) + G_d d,$$

which is simplified further to produce an expression for $y$:

$$\begin{aligned} y &= (1+L)^{-1} L r + (I+L)^{-1} G_d d \\ &= T_c r + S G_d d, \end{aligned} \tag{62}$$

where $K$ is the controller, $L = GK$ is the loop transfer function, $S = (1+L)^{-1}$ is the sensitivity function, $T_c = (1+L)^{-1}L$ is the complimentary sensitivity function, $r = D_e^{-1}\omega_{M\text{ref}}$ is the scaled reference, and the system transfer function is $G = G_W G_M$. The requirement that the maximum allowed output error is not exceeded ($e = r - y < 1$ for $d < 1$), can only be satisfied if (Skogestad & Postlethwaite, 2005):

$$|S(j\omega)| < 1/|G_d(j\omega)| \quad \forall\omega, \tag{63}$$

where $\omega$ denotes frequency. The loop transfer function for the proportional derivative (PD) controller in Fig. 11 is:

$$L_{PD}(s) = \frac{K_P G(s)}{1 + K_D \frac{s}{\tau_D s+1} G(s)}, \tag{64}$$

where $K_P$ is the proportional gain, $K_D$ is the derivative gain, and $\tau_D$ is the derivative filter time constant.

The disturbance rejection requirement of (63) is used to design the PD controller, and is is plotted in Fig. 12. The sensitivity functions indicate that a proportional-only (P) controller violates the disturbance requirement between approximately 55–60 rad/s, whereas the PD controller of (64) meets the requirement. In addition, the loop transfer functions indicate the PD controller is much better at attenuating the resonant peaks and should suppress excessive torsional vibrations.

### 5.3. Rear wheelset PI slip control

Assuming that a slip ratio reference, $\lambda_R$, is provided, the *Wheel Slip Controller* in Fig. 10 should produce a positive reaction torque, $T_{\text{react}}$, during unstable slip ($\hat{\lambda}_{22} > \lambda_R$) of the rear wheelset ($W_{22}$) (Savitski et al., 2018). It may seem reasonable to implement a PD controller again. However, if the slip ratio error is zero, a PD controller will output zero reaction torque, resulting in immediate recurrence of unstable slip. An adaptive PI controller with effective anti-windup, as shown in Fig. 13, is needed to maintain the correct reaction torque.

The transfer function of wheelset from the perspective of the slip controller is:

$$\lambda(s) = \frac{v_{dL}(s) - v_V(s)}{v_V(s)} = G_{\text{slip}}(s)(T^* - T_{\text{react}}(s)), \tag{65}$$

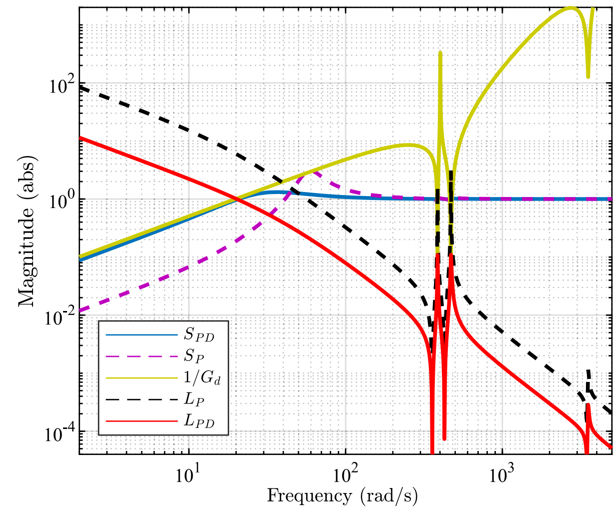


**Fig. 12.** Sensitivity and loop transfer functions of the PD and P controllers and the inverse of the disturbance transfer function.

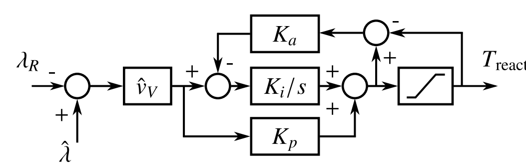


**Fig. 13.** Proportional (gain $K_p$) integral (gain $K_i$) slip controller with anti-windup (gain $K_a$), represented by the Wheel Slip Control block in Figs. 2 and 10.

with:

$$T_{\text{react}}(s) = v_V K_{\text{slip}}(s)(\hat{\lambda}(s) - \lambda_R(s)), \tag{66}$$

where $K_{\text{slip}}(s)$ is the PI slip controller. The PI controller is multiplied by $v_V$ to produce a consistent system response independent of the locomotive velocity (Savitski et al., 2018).

By substituting (66) into (65) and considering the desired torque setpoint, $T^*$, as a disturbance from the perspective of the slip controller ($T^* = 0$):

$$v_{dL} - v_V = v_V G_{\text{slip}} K_{\text{slip}}((v_{dL_R} - v_V) - (v_{dL} - v_V)), \tag{67}$$

which can be written in the form:

$$y = G_{\text{new}} K_{\text{slip}}(r - y). \tag{68}$$

From (68), it can be seen that the model for which the PI controller, $K_{\text{slip}}$, should be designed is:

$$G_{\text{new}} = \frac{v_{dL} - v_V}{T_{\text{react}}} \approx \frac{v_{dL}}{T_{\text{react}}}, \tag{69}$$

where $v_V$ is removed from the model because it can be seen as a constant in this context. The reaction torque, $T_{\text{react}}$, will have an immediate effect on $v_{dL}$, and the locomotive velocity will change at a much slower rate. Therefore, the transfer function for which the PI controller is designed is:

$$G_{\text{new}}(s) = \text{tf}\left(\text{minreal}\left[\begin{array}{c|c} \boldsymbol{A}_w & \boldsymbol{B}_G \\ \hline \boldsymbol{C}_{\text{slip}} & 0 \end{array}\right]\right) G_M(s), \tag{70}$$

with:

$$\boldsymbol{C}_{\text{slip}} = \begin{bmatrix} 0 & 0 & 0 & 0 & r_L & 0 & 0 & 0 \end{bmatrix}, \tag{71}$$

and $\boldsymbol{A}_w$, $\boldsymbol{B}_G$, and $G_M$ defined in (23a), (52), and (61) respectively.

Similar to a gain scheduling approach, two sets of PI gains were designed for the case where $\hat{\lambda}_{22} \le \lambda_R$ (non-slip) and $\hat{\lambda}_{22} > \lambda_R$ (unstable slip). During unstable slip, the wheels slide more freely on the rail, so a given change in torque produces a faster change in wheelset speed. In contrast, during non-slip, the response is slower, allowing for a more aggressive controller. Using a slower controller in the unstable region ensures more consistent behaviour across the transition between non-slip and unstable slip. PI controllers with a 2% settling times of 0.88 s for $\hat{\lambda}_{22} \leq \lambda_R$ and 0.5 s for $\hat{\lambda}_{22} > \lambda_R$ are chosen. The closed-loop poles with either set of gains are all in the left-half plane.

A saturation function ensures that the reaction torque stays positive, $T_{\text{react}} > 0$, which necessitates anti-windup for non-slip conditions ($\hat{\lambda}_{22} \leq \lambda_R$). The anti-windup gain, $K_a$, is usually chosen as the reciprocal of the proportional gain (Kim, 2017). Since anti-windup is only active for $\hat{\lambda}_{22} \leq \lambda_R$, gain scheduling is not needed, and the gain can be set to $K_a = 1/K_{p_{\text{fast}}}$, where $K_{p_{\text{fast}}}$ is the proportional gain $K_p$ of the faster PI controller.

## 6. Slip ratio reference adaptation

As shown in Fig. 2 and discussed in Section 5.3, the slip controller requires a slip ratio reference, $\lambda_R$. Due to the difficulty in generating a reliable slip ratio reference, a constant reference is often used. As mentioned in Section 1, an improvement thereon is creating a peak slip ratio versus locomotive velocity pseudo-static curve, where the peak slip ratios correspond to the peak values of the adhesion coefficient to slip ratio curves shown in Fig. 1 (Kayacan et al., 2009). A lookup table can be constructed to provide the peak slip ratio based on the current locomotive velocity at small velocity intervals. The peak ratios are calculated numerically for a specific adhesion condition from the Polach model as described in Section 3.

Since the pseudo-static curve is generated for a specific adhesion condition, the produced references will not be optimal for all conditions. The proposed improvement is to store multiple pseudo-static curves corresponding to different adhesion levels and to switch between them by detecting the adhesion level.

By using the estimated adhesion coefficient, (49), slip ratio, (50), normal force, (46), and locomotive velocity (second output in (42b)), and comparing with the expected adhesion coefficients for different adhesion levels as shown in Fig. 6, the adhesion level can be detected.

The Polach model in (18) to (22) is summarized as follows:

$$(\mu_{\text{actual}})_n = f_{\text{Polach}}(\{\text{Level}\}_n, \tfrac{1}{2}\hat{F}_N, \hat{\lambda}_{22}, \hat{v}_V), \tag{72}$$

where $\{\text{Level}\}_n$ groups the model parameters $k_A$, $k_S$, $\mu_0$, $A$, and $B$, for the specific adhesion level $n$ of the $N$ adhesion levels ($n \in [0, N]$ where 0 is the lowest adhesion level and $N$ is the highest). The normal force estimate is halved to produce the normal force estimate of a single wheel. Determining the adhesion level is described in Algorithm 1:

**Algorithm 1** Adhesion Level Calculation

1: Initialize the adhesion level $n := N$.
2: Calculate $(\mu_{\text{actual}})_{n+1}$, $(\mu_{\text{actual}})_n$, and $(\mu_{\text{actual}})_{n-1}$ from (72) using $\hat{F}_N$, $\hat{\lambda}_{22}$, and $\hat{v}_V$.
3: UpperLim $:= \frac{1}{2}\left[(\mu_{\text{actual}})_{n+1} + (\mu_{\text{actual}})_n\right]$
   LowerLim $:= \frac{1}{2}\left[(\mu_{\text{actual}})_n + (\mu_{\text{actual}})_{n-1}\right]$
4: **if** $n < N$ **and** $\hat{\mu} >$ UpperLim **then**
5:   $n := n + 1$
6: **else if** $n > 0$ **and** $\hat{\mu} <$ LowerLim **then**
7:   $n := n - 1$
8: **end if**
9: Repeat from step 2.

The calculated level, $n$, determines which pseudo-static slip ratio reference to locomotive velocity curve should be used to produce the reference, $\lambda_R$.

The benefit of this approach is the relative ease of implementation and the reference adaptation is fast (as fast as the adhesion coefficient estimate converges). Even if the wrong adhesion level is identified, a slip ratio reference will be produced that will prevent excessive slip. Due to the discrete nature of the pseudo-static curves and contact dynamics modelling errors, the generated slip ratio reference will not be the exact peak. The peak slip ratio will generally be larger for lower adhesion conditions (Charles et al., 2008). Therefore, identifying a change in adhesion allows the algorithm to produce an adaptive reference superior to a constant reference or a single pseudo-static curve.

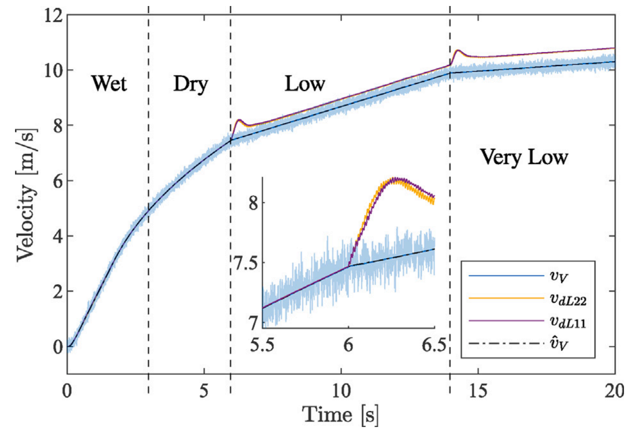


**Fig. 14.** Locomotive velocity, $v_V$, shown with the measured velocity in opaque blue and the estimated velocity in black, alongside the left wheel surface velocities $v_{dLij}$ of the front bogie front wheelset and rear bogie rear wheelset. *Wet*, *Dry*, *Low* and *Very Low* refer to the change in adhesion conditions. (For interpretation of the references to colour in this figure legend, the reader is referred to the web version of this article.)

## 7. Simulation results

### 7.1. Traction

In this simulation, the rail angle is 1° uphill, and the weight of the wagons is 15 ton. The eighth notch is selected (i.e. maximum tractive power). The adhesion conditions are chosen to be *wet* for $t \in [0, 3)$ s, *dry* for $t \in [3, 6)$ s, *low* for $t \in [6, 14)$ s, and *very low* for $t \in [14, 20)$ s to test the slip controller under significant changes in adhesion conditions. The adhesion parameters defined in Charles et al. (2008) are used, while all other model and control parameters are provided in Appendix C. The simulation begins from a standstill because the locomotive can produce the most torque at low velocities, which is expected to cause unstable slip. Zero-mean Gaussian noise with standard deviations of 0.1 m/s and 0.01 m/s$^2$ is added to the locomotive velocity and accelerometer measurements, respectively. The Dormand-Prince solver is used.

Fig. 14 shows the simulation velocity response. During the *wet* and *dry* adhesion conditions, the slip ratio of the rear wheelset is well within the stable/linear region and torque reduction is not needed. However, during the *wet* condition, the front wheelset experiences slip, as can be seen in the slip ratio response in Fig. 15, which the differential speed controller quickly suppresses (within 1.3 s), as can be seen by the reduction in torque, $T_{11}$, in Fig. 16. In addition, Fig. 14 demonstrates that the estimator effectively attenuates measurement noise to produce a smooth velocity estimate.

When the adhesion level drops to the *low* and *very low* conditions, unstable slip occurs (the maximum adhesion point is exceeded). As seen in Fig. 17, the adhesion coefficient changes suddenly when the adhesion level is altered, which causes an error in the adhesion coefficient estimate. However, the estimator converges within 15 ms, which allows for fast detection of changes in the adhesion levels compared to

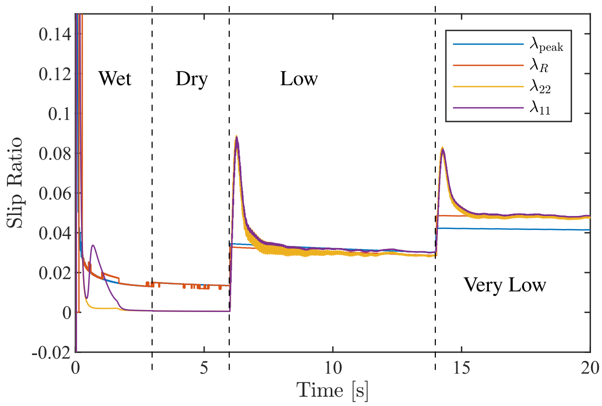


**Fig. 15.** Peak slip ratio reference, $\lambda_{peak}$, calculated slip ratio reference, $\lambda_R$, and the actual slip ratio of the rear bogie rear wheelset, $\lambda_{22}$, and front bogie front wheelset, $\lambda_{11}$.

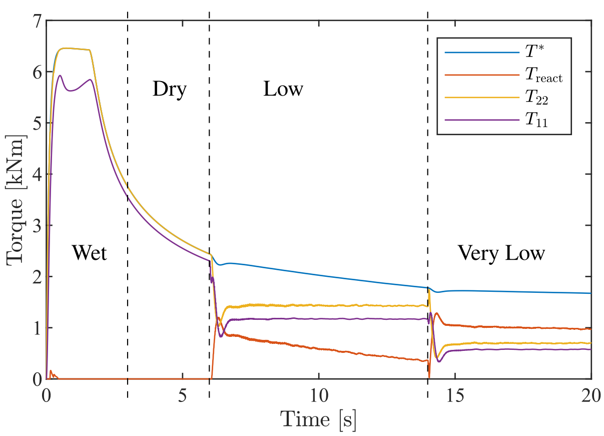


**Fig. 16.** Rear wheelset PI controller torque set-point, $T^*$, reaction torque, $T_{react}$, and applied torque, $T_{22}$, as well as the applied torque of the front wheelset, $T_{11}$, computed with the differential speed controller.

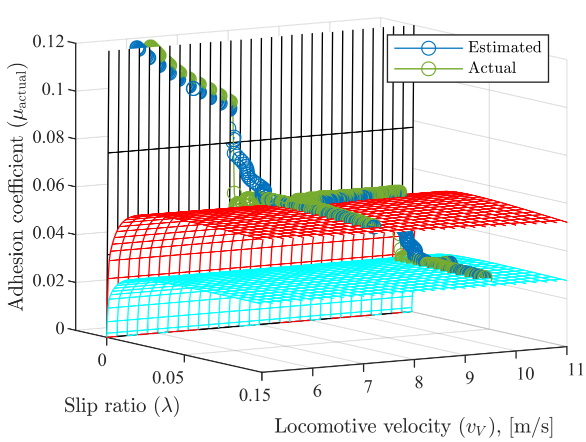


**Fig. 17.** Estimated and actual operating points of the rear bogie rear wheelset plotted onto the *dry* (black), *low* (red), and *very low* (cyan) adhesion conditions. (For interpretation of the references to colour in this figure legend, the reader is referred to the web version of this article.)

the 0.5 s 2% settling time of the slip controller (dictated by mechanical dynamics).

As described in Section 6, the detected adhesion level is used to switch between the pseudo-static curves relating to the desired slip ratios based on the locomotive velocity. Fig. 15 shows that the correct slip ratio reference is detected when unstable slip occurs during *low* adhesion. It is more difficult to determine the adhesion level if the operating point is in the stable region because the adhesion surfaces are close in the stable region. However, an accurate slip ratio reference is only needed during unstable slip.

When the adhesion level drops, unstable slip occurs, and the slip ratio of the rear wheelset, $\lambda_{22}$, overshoots the reference. The slip controller reacts by producing a reaction torque, as shown in Fig. 16, and the unstable slip is suppressed within 1.4 s. After that, the slip controller effectively prevents unstable slip from reoccurring, from which it can be concluded that the anti-windup functions as desired.

As shown in Fig. 15, the reference for the *very low* adhesion is purposefully scaled to exceed the peak reference by 15%. Even though the reference is within the unstable slip region, the slip controller can prevent the slip velocity from increasing uncontrollably. Since operating in the unstable slip region is undesirable, the references used in practice should be less than the peak slip ratios. Using references less than the peak mitigates the torsional vibrations seen in Fig. 15 caused by oscillations of the operating point from the stable to the unstable region.

This simulation has the benefit that the adhesion surfaces used in the adhesion level calculation correspond exactly with those used in the simulation. In reality, capturing the adhesion coefficients produces clouds of points rather than discrete levels. Therefore, this method cannot produce precise slip ratio references, but it provides a method of adapting the reference to a suitable value during varying adhesion conditions. Four discrete levels have been used here, but multiple levels based on experimental data should be constructed in practice. If unstable slip becomes prevalent, the adhesion surfaces used should be retuned so that the slip ratio references are generated more conservatively.

### 7.2. Braking distance

Braking distance simulations were configured to quantify the benefits of slip ratio reference adaptation compared with a constant slip ratio reference, which is often used in many automotive applications (Park et al., 2009; Savitski et al., 2018). For the constant slip ratio reference simulation, a reference of $\lambda_R = 0.01$ was chosen in (66), which is below the peaks of all the adhesion conditions up to 20 m/s, as seen in Fig. 1.

The simulation setup is the same as in Section 7.1, with a few exceptions. The rail angle is 1° downhill. Traction in notch six is applied under dry conditions for 20 s to reach a velocity of 13.5 m/s (a typical operating velocity of a shunting locomotive). After that, the locomotive performs dynamic braking at full power (notch eight) until it reaches a standstill.

Figs. 18 and 19 show the slip ratios with a constant reference and reference adaptation, respectively. The adaptive reference is set to 5% less than the peak. Braking with reference adaptation results in the operating point tracking the peak slip ratio much closer than braking with a constant slip ratio reference. This results in higher adhesion utilization, as seen in Fig. 20. As shown in Table 2, the higher adhesion utilization results in a 3.24% improvement in braking distance. The deviation from the slip ratio references seen in Figs. 18 and 19 after 50 s is due to the large increase in desired torque $T^*$ as the speed nears the crossover velocity described in (B.2).

The simulation is repeated under *very low* adhesion conditions. There is a larger separation between the peak slip ratio and the constant reference, resulting in a significant braking distance reduction of 13.23%.

The smooth adhesion coefficient profile in Fig. 20 differs from experimental estimation results, such as in Hubbard et al. (2024),

**Table 2**
Braking distance improvements under low and very low adhesion conditions.

| Adhesion | Constant | Adaptive | Improvement |
|---|---|---|---|
| *Low* | 306.42 m | 296.49 m | 3.24% |
| *Very Low* | 1379.9 m | 1197.4 m | 13.23% |

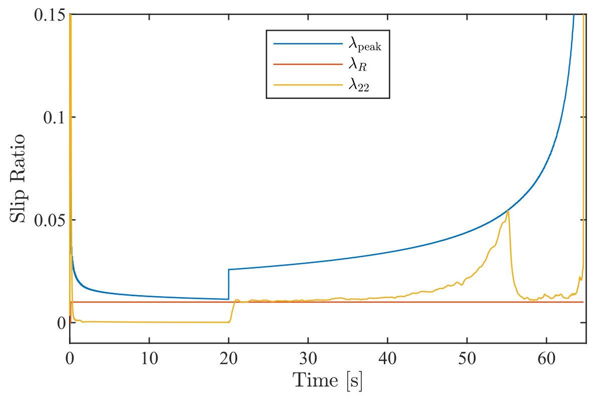


**Fig. 18.** Slip ratios of the rear wheelset during braking with a constant slip ratio reference.

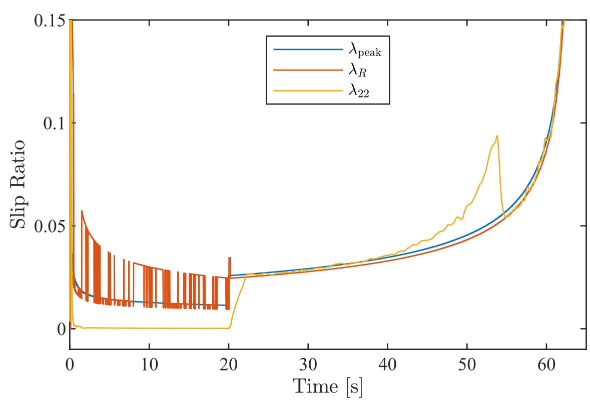


**Fig. 19.** Slip ratios of the rear wheelset during braking with slip ratio reference adaptation.

for two main reasons. Firstly, the controller maintains a slip ratio that maximizes adhesion, intentionally keeping it nearly constant. In contrast, Van de Merwe and Le Roux (2023) report adhesion variations of nearly 100% (from 0.06 at the peak to 0.035 at the minimum) over a 10-s period without such control. Secondly, adhesion is modelled in discrete levels, as shown in Fig. 6, whereas practical tests yield a scatter of data points rather than distinct levels (Pichlik & Zdenek, 2018; Savitski et al., 2018). The results in Fig. 20 are consistent with those obtained in multi-body co-simulation with fixed Polach parameters (Zhao et al., 2023). These idealized conditions allow a clear assessment of the estimator and controller performance under various (discrete) conditions. Results similar to those in Hubbard et al. (2024) could be reproduced by introducing noise to the Polach parameters in (18)–(21), which could be considered in future work.

## 8. Conclusion

This paper addresses various difficulties regarding slip control. The first problem is the difficulty in estimating the adhesion coefficient (needed for slip ratio reference adaptation) and slip ratio (required by the PI controller). The estimator presented in Van de Merwe and Le Roux (2022) and Van de Merwe and Le Roux (2023) addresses this issue by combining a linear model-based estimator for the longitudinal

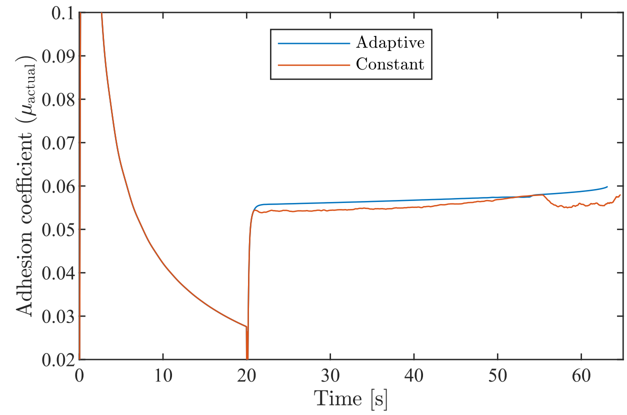


**Fig. 20.** Adhesion coefficients of the rear wheelset, $\mu_{22}$, during braking with slip ratio reference adaptation (adaptive) compared to a constant reference.

and wheelset dynamics with a pitch-plane model to produce the normal force estimates. This paper improves upon the estimator by taking a more rigorous approach to derive the reduced-order wheelset model.

The second problem is that slip ratio reference tracking is difficult because the dynamics (wheelset velocity to input torque response) vary under varying wheel-rail conditions, making PI controllers with constant gains ineffective. The proposed adaptive PI controller with anti-windup, applied to the rear wheelset, offers a simple and effective solution. The reference tracking could be further improved by using controllers such as SMC or MPC, which warrants further investigation in future work. By ensuring that the wheelset with the largest normal force does not slip (generally the rear wheelset), slip in the other wheelsets is easily prevented with a differential speed controller that tracks the speed of the reference (rear) wheelset.

The final problem is that the peak/maximum adhesion point is unknown and shifts with a change in wheel-rail conditions. In automotive applications, a constant slip ratio reference is often used. A new slip ratio reference adaptation algorithm is presented, which generates a slip ratio reference based on the detected adhesion level. The adhesion level is detected by comparing the estimated and expected adhesion coefficient for different adhesion levels at the estimated adhesion ratio and locomotive velocity. The adhesion coefficient estimate converges within 15 ms, enabling fast detection of the adhesion level. The slip ratio reference adaptation is straightforward to implement and improves the braking distance by up to 13% compared to a constant reference.

The proposed system is suitable for practical implementation on modern locomotives. It effectively maximizes adhesion utilization while preventing excessive unstable slip.

## CRediT authorship contribution statement

**Charl V. van de Merwe:** Writing – review & editing, Writing – original draft, Visualization, Validation, Software, Methodology, Investigation, Formal analysis, Conceptualization. **Johan D. le Roux:** Writing – review & editing, Visualization, Validation, Supervision, Methodology, Formal analysis. **David J.N. Limebeer:** Writing – review & editing, Visualization, Validation, Supervision, Formal analysis, Conceptualization.

## Declaration of competing interest

The authors declare that they have no known competing financial interests or personal relationships that could have appeared to influence the work reported in this paper.

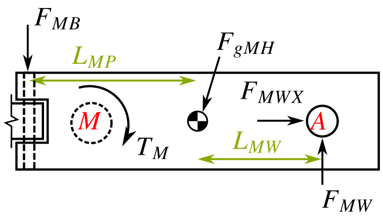


**Fig. A.21.** Forces on the motor housing. The motor housing contains the motor (at $M$), pinion, gear wheel, and wheelset axle (at $A$). It is fixed to the bogie with the vertical pin (shown as dashed lines to the left of $M$).

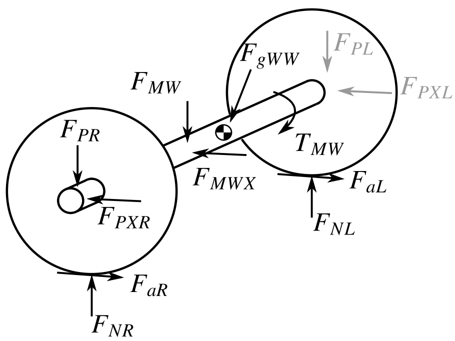


**Fig. A.22.** Forces on the wheelset.

## Appendix A. Normal forces

The force between the motor housing and the bogie, $F_{MBij}$, is derived for any wheelset $ij$ by assuming that the motor housing shown in Fig. A.21 has no pitch. Therefore, the vertical displacement of the housing is equal to the vertical displacement of the wheelset, and the moments around the axle bearings in the motor housing are zero:

$$F_{MBij} = \frac{1}{L_{MP}+L_{MW}} T_{Mij} - \frac{L_{MW}}{L_{MP}+L_{MW}} F_{gMHij} \cos\beta, \tag{A.1}$$

where $F_{gMHij}$ is the gravitational force of the motor and housing, and $T_{Mij}$ is the torque from the motor on the housing.

To calculate the normal force on the wheelset, as shown in Fig. A.22, the vertical forces on the motor housing in Fig. A.21 are considered first (ignoring the $ij$ subscripts for brevity):

$$m_{MH}\ddot{z}_W = F_{MB} + F_{gMH}\cos\beta - F_{MW}, \tag{A.2}$$

where $m_{MH}$ is the mass of the motor and motor housing, $F_{MB}$ is the force from the housing to the bogie, and $F_{MW}$ is the force from the housing to the wheelset. It is assumed that the wheelset never loses contact with the rail and that the changes in the rail angle occur slowly. Therefore, the vertical acceleration of the wheelset, $\ddot{z}_W$, is assumed to be zero. By substituting (A.1) into (A.2) the housing to wheelset force is:

$$F_{MW} = \frac{1}{L_{MP}+L_{MW}} T_M + \frac{L_{MP}}{L_{MP}+L_{MW}} F_{gMH}\cos\beta. \tag{A.3}$$

The normal force on a wheelset is determined from the vertical forces on the wheelset in Fig. A.22:

$$m_{WW}\ddot{z}_W = F_P + F_{MW} + F_{gWW}\cos\beta - F_N, \tag{A.4}$$

where $m_{WW}$ is the mass of the wheelset without the motor, $F_N$ is the sum of the left and right normal forces ($F_{NL}$ and $F_{NR}$) on the wheels, $F_P$ is the sum of the left and right vertical primary suspension forces ($F_{PL}$ and $F_{PR}$), and $F_{gWW}$ is the gravitational force. By substituting (A.3) into (A.4) and assuming that $\ddot{z}_W = 0$, the normal force for any wheelset $ij$ is:

$$F_{Nij} = F_{Pij} + \frac{1}{L_{MP}+L_{MW}} T_{Mij} + \left(\frac{L_{MP}}{L_{MP}+L_{MW}} F_{gMHij} + F_{gWWij}\right)\cos\beta. \tag{A.5}$$

In this simulation model, the left and right wheel normal forces are equal, i.e. $F_{NLij} = F_{NRij} = \frac{1}{2}F_{Nij}$.

## Appendix B. Tractive effort and motor torque

The locomotive operator sets the required tractive effort by selecting the throttle notch. A diesel-electric locomotive typically has eight notches (levels) of throttle adjustment (Iwnicki, 2006).

The traction system is current limited at low velocities and power limited at higher velocities. Accordingly, the tractive effort command, $F_t$, can be calculated as follows (Spiryagin et al., 2017):

$$F_t = \begin{cases} (N/8)\,F_{\max} - k_f v_d & ; \quad v_d < v_{\text{cross}} \\ (N/8)^2\,P_{\max}/v_d & ; \quad \text{otherwise}, \end{cases} \tag{B.1}$$

with:

$$v_{\text{cross}} = \frac{(N/8)F_{\max} - \sqrt{((N/8)F_{\max})^2 - 4k_f P_{\max}(N/8)^2}}{2k_f}, \tag{B.2}$$

where $v_d$ is the wheel velocity at the wheel-rail contact point, $v_{\text{cross}}$ is the crossover velocity after which the system is limited by power, $F_t$ is the tractive effort command, $F_{\max}$ is the maximum tractive effort that the locomotive can produce, $P_{\max}$ is the maximum locomotive tractive power, $N$ is the notch level selected, and $k_f$ is the torque reduction factor.

For individual wheelset control, the desired torque of a single wheelset is calculated by:

$$T^* = \frac{r}{n_a R} F_t, \tag{B.3}$$

where $T^*$ is the motor torque setpoint, as shown in Figs. 2 and 10, $r$ is the distance from the axle centre to the wheel-rail contact surface (wheel radius), $n_a$ is the axle count of the locomotive, and $R$ is the gear ratio of the gearbox (Spiryagin et al., 2017).

## Appendix C. Model parameters

The complete set of parameter values used in the simulations is reported in Van de Merwe (2023). For brevity, these values are reproduced in Tables C.3 and C.4 without accompanying descriptions, which are provided in the text.

**Table C.3**
Controller parameters.

| Symbol | Value | Symbol | Value |
|---|---|---|---|
| $\tau_{LPF}$ | 0.8 s | $K_P$ | 1000 N s/rad |
| $K_D$ | 20 N s$^2$/rad | $\tau_D$ | 0.001 s |
| $K_p$ | 2261.9 N s/m | $K_i$ | 5055.3 N/m |
| $K_{p\text{fast}}$ | 4090.6 N s/m | $K_{i\text{fast}}$ | 32.12 × 10$^3$ N/m |
| $K_{a\text{fast}}$ | 244.5 × 10$^{-6}$ m/s/N | | |

**Table C.4**
Model parameters.

| Sym. | Value | Sym. | Value |
|---|---|---|---|
| $m_V$ | 62 120 kg | $m_{B1}$ | 11 000 kg |
| $m_{B2}$ | 11 000 kg | $m_{Wij}$ | 3400 kg |
| $m_A$ | 24 430 kg | $m_L$ | 97 720 kg |

(continued on next page)

**Table C.4** (*continued*).

| Sym. | Value | Sym. | Value |
|---|---|---|---|
| $I_V$ | 3 793 457 kg m$^2$ | $I_{B1}$ | 33 585 kg m$^2$ |
| $I_{B2}$ | 33 585 kg m$^2$ | $I_L$ | 154 kg m$^2$ |
| $I_R$ | 154.1 kg m$^2$ | $I_G$ | 24.982 kg m$^2$ |
| $I_P$ | 0.161 kg m$^2$ | $I_M$ | 16.205 kg m$^2$ |
| $k_1$ | 30.15 × 10$^6$ N m/rad | $k_2$ | 21.12 × 10$^6$ N m/rad |
| $k_3$ | 7.382 × 10$^6$ N m/rad | $k_{Pij}$ | 782 × 10$^3$ N/m |
| $k_{PXij}$ | 101.5 × 10$^6$ N/m | $k_{Sij}$ | 20 × 10$^6$ N/m |
| $k_{Ti}$ | 25 × 10$^6$ N/m | $c_1$ | 100.5 N m s/rad |
| $c_2$ | 70.4 N m s/rad | $c_3$ | 24.6 N m s/rad |
| $c_{Pij}$ | 50 × 10$^3$ N s/m | $c_{Sij}$ | 50 × 10$^6$ N s/m |
| $c_{Ti}$ | 1 × 10$^6$ N s/m | $r_L, r_R$ | 0.61 m |
| $H_{VT}$ | 1.0 m | $H_C$ | 0.8 m |
| $H_{BT}$ | 0.2 m | $H_P$ | 0.3 m |
| $H_{BR}$ | 0.795 m | $H_{CT}$ | 0.2 m |
| $H_{TR}$ | 1.11 m | $L_{MBij}$ | 0.24 m |
| $L_{B1}$ | 4.425 m | $L_{B2}$ | 3.425 m |
| $L_C$ | 7.56 m | $L_{Pij}$ | 1.64 m |
| $L_{Sij}$ | 0.3 m | $L_{V11}$ | 4.725 m |
| $L_{V12}$ | 4.125 m | $L_{V21}$ | 3.125 m |
| $L_{V22}$ | 3.725 m | $L_{MP}$ | 0.5 m |
| $L_{MW}$ | 0.9 m | $R$ | 115/17 m |
| $L_{VT1}$ | 4.425 m | $L_{VT1}$ | 3.425 m |
| $L_{BNij}$ | 1.64 m | $F_{max}$ | 287.6 × 10$^3$ N |
| $P_{max}$ | 800 × 10$^3$ W | $n$ | 4 |
| $k_f$ | 1000 N s/m | $n_W$ | 1 |
| $\tau_M$ | 0.05 s | $m_W$ | 15 000 kg |
| $I_W$ | 1600 kg m$^2$ | $k_C$ | 100 × 10$^6$ N/m |
| $c_C$ | 300 × 10$^6$ N s/m | | |

## References


Ararat, Ö., & Söylemez, M. T. (2017). Robust velocity estimation for railway vehicles. *IFAC-PapersOnLine*, *50*(1), 5961–5966. http://dx.doi.org/10.1016/j.ifacol.2017.08.1256.

Berntorp, K. (2016). Joint wheel-slip and vehicle-motion estimation based on inertial, GPS, and wheel-speed sensors. *IEEE Transactions on Control Systems Technology*, *24*(3), 1020–1027. http://dx.doi.org/10.1109/TCST.2015.2470636.

Caporale, D., Colaneri, P., & Astolfi, A. (2013). Adaptive nonlinear control of braking in railway vehicles. In *52nd IEEE Conference on Decision and Control* (pp. 6892–6897). http://dx.doi.org/10.1109/CDC.2013.6760981.

Chang, C., Chen, B., Cai, Y., & Wang, J. (2019). An experimental study of high speed wheel-rail adhesion characteristics in wet condition on full scale roller rig. *Wear*, *440–441*, Article 203092. http://dx.doi.org/10.1016/j.wear.2019.203092.

Charles, G., Goodall, R., & Dixon, R. (2006). Wheel-rail profile estimation. In *2006 IET International Conference on Railway Condition Monitoring* (pp. 32–37).

Charles, G., Goodall, R., & Dixon, R. (2008). Model-based condition monitoring at the wheel–rail interface. *Vehicle System Dynamics*, *46*(sup1), 415–430. http://dx.doi.org/10.1080/00423110801979259.

Djukić, M., Rusov, S., & Mitrović, Z. (2010). A fuzzy model for an increase in locomotive traction force. *Transport*, *25*(1), 36–45. http://dx.doi.org/10.3846/transport.2010.06.

Glover, K. (1984). All optimal Hankel-norm approximations of linear multivariable systems and their $L_\infty$ -error bounds. *International Journal of Control*, *39*(6), 1115–1193. http://dx.doi.org/10.1080/00207178408933239.

Green, M., & Limebeer, D. J. N. (2012). *Linear robust control* (second ed.). Newburyport: Dover.

Grewal, M. S., & Andrews, A. P. (2015). *Kalman filtering: Theory and practice using MATLAB* (fourth ed.). Hoboken, New Jersey: John Wiley & Sons, Inc..

He, J., Liu, G., Liu, J., Zhang, C., & Cheng, X. (2018). Identification of a nonlinear wheel/rail adhesion model for heavy-duty locomotives. *IEEE Access*, *6*, 50424–50432. http://dx.doi.org/10.1109/ACCESS.2018.2868177.

Hubbard, P. D., Amarantidis, G. A., & Ward, C. P. (2016). Leaves on the line: Low adhesion detection in railways. *IFAC-PapersOnLine*, *49*(21), 467–472. http://dx.doi.org/10.1016/j.ifacol.2016.10.647.

Hubbard, P., Harrison, T., Ward, C. P., & Abduraxman, B. (2024). Creep slope estimation for assessing adhesion in the wheel/rail contact. *IET Intelligent Transportation System*, *18*(10), 1931–1942. http://dx.doi.org/10.1049/itr2.12561.

Iwnicki, S. (2006). *Handbook of railway vehicle dynamics*. Boca Raton: CRC/Taylor & Francis.

Kalker, J. J. (1990). *Three-dimensional elastic bodies in rolling contact*. Dordrecht, Netherlands: Kluwer Academic Publishers.

Kayacan, E., Oniz, Y., & Kaynak, O. (2009). A grey system modeling approach for sliding-mode control of antilock braking system. *IEEE Transactions on Industrial Electronics*, *56*(8), 3244–3252. http://dx.doi.org/10.1109/TIE.2009.2023098.

Kim, S.-H. (2017). *Electric motor control*. Amsterdam, Netherlands: Elsevier Inc..

Kun, D., Kaijun, L., & Qunsheng, X. (2006). Application of unscented Kalman filter for the state estimation of anti-lock braking system. In *2006 IEEE International Conference on Vehicular Electronics and Safety* (pp. 130–133). http://dx.doi.org/10.1109/ICVES.2006.371568.

Mei, T. X., & Li, H. (2010). Measurement of absolute vehicle speed with a simplified inverse model. *IEEE Transactions on Vehicular Technology*, *59*(3), 1164–1171. http://dx.doi.org/10.1109/TVT.2010.2040199.

Ndiaye, A. W., Cassaro, M., Combier, C., Biannic, J.-M., & Roos, C. (2022). On-ground aircraft modeling for advanced braking control system design. In *2022 European Control Conference* (pp. 649–656). http://dx.doi.org/10.23919/ECC55457.2022.9838377.

Ohishi, K., Nakano, K., Miyashita, I., & Yasukawa, S. (1998). Anti-slip control of electric motor coach based on disturbance observer. In *5th International Workshop on Advanced Motion Control* (pp. 580–585).

Park, S. H., Kim, J. S., & Choi, J. J. (2009). Reference slip ratio generation and adaptive sliding mode control for railway rolling stocks. *International Journal of Precision Engineering and Manufacturing*, *10*(2), 39–44. http://dx.doi.org/10.1007/s12541-009-0025-0.

Picasso, B., Caporale, D., & Colaneri, P. (2018). Braking control in railway vehicles: A distributed preview approach. *IEEE Transactions on Automatic Control*, *63*(1), 189–195. http://dx.doi.org/10.1109/TAC.2017.2725480.

Pichlik, P. (2019). Locomotive wheel slip controller based on power dissipation in wheel-rail contact. In *2019 International Conference on Electrical Drives & Power Electronics* (pp. 211–216). http://dx.doi.org/10.1109/EDPE.2019.8883900.

Pichlik, P., & Zdenek, J. (2018). Locomotive wheel slip control method based on an unscented Kalman filter. *IEEE Transactions on Vehicular Technology*, *16*(7), 5730–5739. http://dx.doi.org/10.1109/TVT.2018.2808379.

Polach, O. (2005). Creep forces in simulations of traction vehicles running on adhesion limit. *Wear*, *258*, 992–1000. http://dx.doi.org/10.1016/j.wear.2004.03.046.

Pretagostini, F., Ferranti, L., Berardo, G., Ivanov, V., & Shyrokau, B. (2020). Survey on wheel slip control design strategies, evaluation and application to antilock braking systems. *IEEE Access*, *8*, 10951–10970. http://dx.doi.org/10.1109/ACCESS.2020.2965644.

Reitmann, E. (2017). *19E vibration investigation – wheel tread polygonisation caused by self-excited torsional vibration: Technical report*, Transnet Freight Rail.

Rezaeian, A., Zarringhalam, R., Fallah, S., Melek, W., Khajepour, A., Chen, S.-K., Moshchuck, N., & Litkouhi, B. (2015). Novel tire force estimation strategy for real-time implementation on vehicle applications. *IEEE Transactions on Vehicular Technology*, *64*(6), 2231–2241. http://dx.doi.org/10.1109/TVT.2014.2345695.

Ronanki, D., Singh, S. A., & Williamson, S. S. (2017). Comprehensive topological overview of rolling stock architectures and recent trends in electric railway traction systems. *IEEE Transactions on Transportation Electrification*, *3*(3), 724–738. http://dx.doi.org/10.1109/TTE.2017.2703583.

Sadr, S., Khaburi, D. A., & Rodriguez, J. (2016). Predictive slip control for electrical trains. *IEEE Transactions on Industrial Electronics*, *63*(6), 3446–3457. http://dx.doi.org/10.1109/TIE.2016.2543180.

Savitski, D., Schleinin, D., Ivanov, V., & Augsburg, K. (2018). Robust continuous wheel slip control with reference adaptation: Application to the brake system with decoupled architecture. *IEEE Transactions on Industrial Informatics*, *14*(9), 4212–4223. http://dx.doi.org/10.1109/TII.2018.2817588.

Skogestad, S., & Postlethwaite, I. (2005). *Multivariable feedback control: Analysis and design*. Hoboken, NJ, USA: John Wiley & Sons, Inc..

Spiryagin, M., Sun, Y. Q., Cole, C., Simson, S., & Persson, I. (2011). Development of traction control for hauling locomotives. *Journal of Dynamical and Control Systems*, *5*(6), 1214–1225. http://dx.doi.org/10.1299/jsdd.5.1214.

Spiryagin, M., Wolfs, P., Cole, C., Spiryagin, V., Sun, Y. Q., & McSweeney, T. (2017). *Design and simulation of heavy Haul locomotives and trains*. Boca Raton: CRC/Taylor & Francis.

Tavernini, D., Vacca, F., Metzler, M., Savitski, D., Ivanov, V., Gruber, P., Hartavi, A. E., Dhaens, M., & Sorniotti, A. (2020). An explicit nonlinear model predictive ABS controller for electro-hydraulic braking systems. *IEEE Transactions on Industrial Electronics*, *67*(5), 3990–4001. http://dx.doi.org/10.1109/TIE.2019.2916387.

Tian, Y., Daniel, W. J. T., Liu, S., & Meehan, P. A. (2014). Fuzzy logic creep control for a 2D locomotive dynamic model under transient wheel-rail contact conditions. In *Computers in Railways XIV* (pp. 885–896). http://dx.doi.org/10.2495/CR140741.

Van de Merwe, C. V. (2023). *Model-based estimation and control of wheel slip in locomotives* (Masters dissertation), Pretoria, South Africa: University of Pretoria, URL: http://hdl.handle.net/2263/103971.

Van de Merwe, C. V., & Le Roux, J. D. (2022). Model-based estimation of wheel slip in locomotives. In *2022 European Control Conference* (pp. 2124–2129). http://dx.doi.org/10.23919/ECC55457.2022.9838075.

Van de Merwe, C. V., & Le Roux, J. D. (2023). Estimation of locomotive adhesion coefficients and slip ratios. In *American Control Conference* (pp. 2252–2257). http://dx.doi.org/10.23919/ACC55779.2023.10155953.

Wang, S., Xiao, J., Huang, J., & Sheng, H. (2016). Locomotive wheel slip detection based on multi-rate state identification of motor load torque. *Journal of the Franklin Institute*, *353*(2), 521–540. http://dx.doi.org/10.1016/j.jfranklin.2015.11.012.

Wang, S., Zhang, W., Huang, J., Wang, Q., & Sun, P. (2019). Adhesion control of heavy-duty locomotive based on axle traction control system. *IEEE Access*, *7*, 164614–164622. http://dx.doi.org/10.1109/ACCESS.2019.2952268.

Ward, C. P., Goodall, R. M., & Dixon, R. (2011). Contact force estimation in the railway vehicle wheel-rail interface. *IFAC Proceedings Volumes*, *44*(1), 4398–4403. http://dx.doi.org/10.3182/20110828-6-IT-1002.02904.

Ward, C. P., Goodall, R. M., Dixon, R., & Charles, G. A. (2012). Adhesion estimation at the wheel–rail interface using advanced model-based filtering. *Vehicle System Dynamics*, *50*(12), 1797–1816. http://dx.doi.org/10.1080/00423114.2012.707782.

Yasuoka, I., Mochizuki, Y., Toda, S.-I., Nakazawa, Y., Hongguang, G., & Huiyan, L. (2009). Consideration of wheel slip and readhesion control for induction traction motor electric locomotives with individual traction control. *Electrical Engineering in Japan*, *169*(3), 55–64. http://dx.doi.org/10.1002/eej.20883.

Zengin, N., Zengin, H., Fidan, B., & Khajepour, A. (2020). Slip ratio optimization in vehicle safety control systems using least-squares based adaptive extremum seeking. In *2020 IEEE International Conference on Systems, Man, and Cybernetics* (pp. 1445–1450). http://dx.doi.org/10.1109/SMC42975.2020.9283109.

Zhao, Y., Shen, L., Jiang, Z., Zhang, B., Liu, G., Shu, Y., & Peng, B. (2023). Real-time wheel–rail friction coefficient estimation and its application. *Vehicle System Dynamics*, *61*(10), 2598–2612. http://dx.doi.org/10.1080/00423114.2022.2159846.